UNIVERSITAT POLITÈCNICA DE VALÈNCIA

ESCUELA TÉCNICA SUPERIOR INGENIERÍA INDUSTRIAL VALENCIA

TRABAJO FIN DE GRADO EN INGENIERÍA BIOMÉDICA

CHARACTERIZATION OF MOLECULAR MONOLAYERS ON PHOTONIC NANOSTRUCTURES FOR INTEGRATED THZ DETECTORS

AUTHORESS: MARÍA CAMARENA PÉREZ

SUPERVISOR: ALEJANDRO JOSÉ MARTÍNEZ ABIETAR

SUPERVISOR: ELENA PINILLA CIENFUEGOS

Academic year: **2021-22**

Acknowledgments

To begin with, I would like to express my gratitude to Prof. Alejandro José Martínez Abietar for his confidence in me from the very beginning and for giving me the unique opportunity to undertake my Final Degree Project at the NTC. It was certainly an unforgettable experience that I will always remember with joy.

I would also like to express my warmest thanks to Elena Pinilla Cienfuegos. I can't thank you enough for everything you have taught me, both academically and personally. You have certainly made this journey way easier and enjoyable. Always continue bringing value to the scientific community with the enthusiasm and joy that characterizes you.

I want to extend my sincere thanks to all my NTC colleagues, and especially Javi, Fran and Evelyn, who have always supported me in everything I have needed.

Finally, I would like to thank Iñigo and my parents for their overwhelming support and trust. You are my fundamental support.

Abstract

Combining plasmonics and molecular optomechanics is proving to be a potentially promising approach for the development of integrated THz sensors which allow the coupling of this signal to the visible spectrum, providing a new range of diagnostic opportunities that are virtually innocuous for the patient. Raman spectroscopy is a key issue here, as it offers the possibility to detect the resulting signal coupling. Therefore, the development of new experimental methodologies is essential to generate and characterize the nanophotonic structures that will compose these THz detectors. In this work, two types of molecules have been used to functionalize the plasmonic surfaces, which allow the coupling of signals in these frequency ranges. These are Biphenyl-4-thiol (BPT) and 5-amino-2-mercaptobenzimidazole (ABIZ), having developed a new surface functionalization technique for the latter. In order to generate the plasmonic structures, gold nanoparticles (NPs) have been deposited on the surface of lithographed structures by two methodologies, one of them being a new NPs transfer technique called micro-contact printing. These structures have been successfully characterized using different techniques. A new experimental setup has also been assembled to perform Waveguide Enhanced Raman Spectroscopy (WERS), which is important to simulate the wave-guiding conditions, as well as to characterize such circuits. Finally, simulations have been performed to determine possible new photonic nanostructures for signal coupling.

Keywords: Raman spectroscopy, Nanoparticle (NP), SERS, WERS, Functionalization, BPT, ABIZ, SAM, molecular optomechanics.

Resumen

La combinación de la plasmónica y la optomecánica molecular está demostrando ser un campo potencialmente prometedor para el desarrollo de sensores de THz integrados que permiten acoplar esta señal a la del espectro visible, proporcionando un nuevo abanico de oportunidades de diagnóstico prácticamente inocuo para el paciente. La espectroscopia Raman es un aspecto clave en este caso, ya que ofrece la posibilidad de detectar la señal resultante del acople de señales. Por ello, el desarrollo de nuevas metodologías experimentales es esencial para generar y caracterizar las estructuras nanofotónicas que compondrán estos detectores de THz. En este trabajo, se han utilizado dos tipos de moléculas para funcionalizar las superficies plasmónicas, las cuales permiten el acoplamiento de señales en estos rangos de frecuencia. Estas son el Biphenil-4-tiol (BPT) y el 5-amino-2- mercaptobenzimidazole (ABIZ), habiendo desarrollado para esta última nueva técnica de funcionalización de superficies. Para generar las estructuras plasmónicas, se han depositado nanopartículas (NPs) de oro en la superficie de estructuras litografiadas mediante dos metodologías, siendo una de ellas una nueva técnica de transferencia de NPs que se ha denominado *micro-contact printing*. Estas estructuras han sido caracterizadas con éxito mediante distintas técnicas. También se ha ensamblado un nuevo setup experimental para realizar Espectroscopia Raman mejorada por guía de ondas (WERS), lo cual es importante para simular las condiciones de guiado de la onda, así como para caracterizar dichos circuitos. Por ultimo, se han realizado simulaciones para determinar posibles estructuras plasmónicas nuevas que permitan el acoplamiento de las señales.

Palabras clave: Espectroscopía Raman, Nanopartícula (NP), SERS, WERS, Funcionalización, BPT, ABIZ, SAM, optomecánica molecular.

Resum

La combinació de la plasmónica i l'optomecánica molecular està demostrant ser un camp potencialment prometedor per al desenrotllament de sensors de THz integrats que permeten acoblar este senyal a la de l'espectre visible, proporcionant un nou palmito d'oportunitats de diagnòstic pràcticament innocu per al pacient. L'espectroscòpia Raman és un aspecte clau en este cas, ja que oferix la possibilitat de detectar el senyal resultant de l'acoble de senyals. Per això, el desenrotllament de noves metodologies experimentals és essencial per a generar i caracteritzar les estructures nanofotónicas que compondran estos detectors de THz. En aquest treball, s'han utilitzat dos tipus de molècules per a funcionalizar les superfícies plasmòniques, les quals permeten l'adaptament de senyals en estos rangs de freqüència. Estes són el Biphenil-4-tiol (BPT) i el 5-amino-2-mercaptobenzimidazole (ABIZ), havent desenvolupat per a aquesta última una nova tècnica de funcionalització de superfícies. Per a generar les estructures plasmòniques, s'han depositat nanopartículas (NPs) d'or en la superfície d'estructures litografiades per mitjà de dos metodologies, sent una d'elles una nova tècnica de transferència de NPs que s'ha denominat *micro-contact printing*. Estes estructures han sigut caracteritzades amb èxit per mitjà de distintes tècniques. També s'ha generat un nou setup experimental per a realitzar Espectroscòpia Raman millorada per guia d'ones (WERS), la qual cosa és important per a simular les condicions de guiat de l'onda, així com per a caracteritzar els mencionats circuits. Per últim, s'han realitzat simulacions per a determinar possibles estructures plasmòniques noves que permeten l'adaptament de les senyals

Paraules clau: Espectroscòpia Raman, Nanopartícula (NP), SERS, WERS, Funcionalització, BPT, ABIZ, SAM, optomecánica molecular.

Contents

Acronyms

ABIZ 5-Amino-2-mercaptobenzimidazole

BPT Biphenyl-4-thiol

DLS Dynamic Light Scattering

IR Infrared

LSPR Localized Surface Plasmonic Resonance

NP Nanoparticle

NPoM Nanoparticle on Mirror

PDMS polydimethylsiloxane

SAM Self Assembled Monolayer

SERS Surface Enhanced Raman Spectroscopy

SPR Surface Plasmon Resonance

WERS Wave-guided Enhanced Raman Spectroscopy

List of Figures

Part I

Memory

Chapter 1

INTRODUCTION

1.1 Motivation and justification

Over the last decades the evolution of technology has allowed the development of novel techniques based on the emission, detection and analysis of the electromagnetic spectrum signals. Up to now, the exploitation of these techniques has successfully addressed several areas, including data transmission, imaging acquisition, sensing, lighting, among others. Although it has been possible to perform excellent results operating with most of the electromagnetic spectrum, the scarcity of detectors and components to manipulate the Infrared (IR) signals constitutes what is commonly known as the THz gap [1]. This gap includes the frequencies between 0.1 and 30 THz, a frequency range that provides significant information in many areas, from telecommunications to space flight missions [2]. In terms of biomedical applications, the THz frequency band delivers relevant information for biomedical imaging, biomolecular dynamics, biosensors, biomedical therapies and biomedical diagnosis [3]. The shallow penetration depth of the IR makes it more harmless than radio-frequency or microwave, constituting an unparalleled innocuous technique [4, 5].

In recent years, efforts have been made in order to ”fill” the THz Gap due to the potential information the IR spectroscopy provides. To date, techniques as Fourier-Transform IR (FTIR) and tunable laser sources have proved useful for infrared spectroscopy [6]. However, these methods generally have to deal with a greater noise effects than near-infrared and visible detectors [7]. Other State of the Art detectors require low operating temperatures, resulting in lower cost-effectiveness ratios. [8]. Considering these constraints, the production of detectors that can operate effectively both in low noise and at ambient temperature remains a challenge [9].

State of the Art

Currently, the exceptional progress of nanotechnology allows solutions to be considered from a nanoscale perspective. One of the fast-growing fields is the development of plasmonic biosensors, whose operation is based on the interaction of light with certain metallic surfaces and nanostructures of similar size to its wavelength [10, 11]. Combining plasmonic structures with molecular optomechanics

results in the possibility of detecting IR radiation through frequency up-conversion enabled by molecular optomechanical coupling [12]. This combination can be performed through plasmonic surface functionalization, where the meaning of functionalize is to create a Self Assembled Monolayer (SAM) on a particular structure. Figure 1.1 shows the big picture of molecular up-conversion. The basis of this phenomenom lies in using molecules with both high THz and Raman (visible) vibrational activity, which allows consistent energy transfer and consequent up-conversion [13]. The output of the system results from the coupling of both input signals, thus enabling the detection of the THZ.

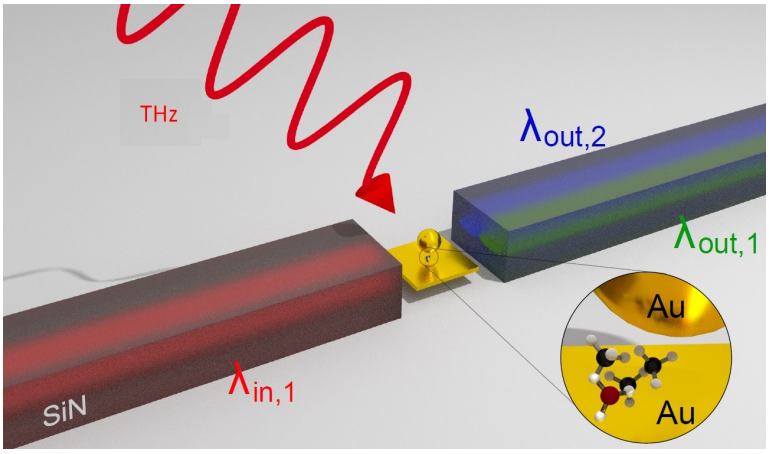

Figure 1.1: Functionalized plasmonic nanocavity integrated with silicon guides to perform frequency up-conversion. Image from THOR project.

As can be seen in figure 1.1, a gold Nanoparticle (NP) linked to a gold surface is used to create a plasmonic structure to enhance the output signal. The attachment of plasmonic structures is performed using the molecules as a link. Both input and output signals can be guided, allowing the integration of photonic circuits on chips, increasing the cost-effective ratio and providing fast, low-noise results at room temperature [14]. It is necessary to emphasise that only particular molecules meet the specific requirements that enable up-conversion. Therefore, it is essential the study and characterization of these molecules, as well as the characterization of the plasmonic structures that will interact with them. Furthermore, developing new techniques to characterise this particular nanophotonic circuits is also a requirement.

The present work focuses on the characterization of molecular monolayers, commonly know as Self Assembled Monolayer (SAM), that allow signal up-conversion, from their production to their validation, using new synthesis and experimental techniques. In addition, potential photonic circuits where the molecules are integrated have also been studied and characterised. Finally, a new wave-guided Raman system has been assembled, which is useful for studying the photonic structures and ensuring their future assembly in integrated circuits.

1.2 Objectives

The main purpose of this work is to characterise the SAMs performed in several nanophotonic circuits, in order to demonstrate and validate new functionalization and experimental techniques developed in the course of the work and which will be explained in the following chapters. The feasibility and stability of the SAMs will be probed, among others, by surface NPs deposition, which characterization will also be necessary. In order to ensure that the general objective is met, some specific objectives (SO) mentioned below need to be fulfilled:

- **SO1**. Design and manufacturing of nanophotonic structures. Performing simulations to study the SAM thickness effect; study of simulations and manufacture of the different types of plasmonic structures used in this work.
- **SO2**. Surface functionalization: performing and characterizing surface functionalization in the laboratory with known molecules Biphenyl-4-thiol (BPT) and new molecules 5-Amino-2-mercaptobenzimidazole (ABIZ) that allow up-conversion.
- **SO3**. Transfer of gold nanoparticles onto functionalized surfaces to achieve light confinement in the monolayer.
- **SO4**. Wave-guide Enhanced Raman Spectroscopy setup assembly, with the aim of developing characterization techniques under guidance (to develop integrated sensors, lab-on-a-chip).
- **SO5**. Simulation of other potential circuits for future work using CST STUDIO SUITE, which includes learning and developing simulations to study new photonic circuit configurations.

The distribution of the tasks associated with these objectives is shown in figure 1.2 and the experimental implementation of these is explained in Chapter 3.

SPECIFIC OBJECTIVES		November				December				January				February				March				April				May		
WEEK		1	2	3	4	1	2	3	4	1	2	3	4	1	2	3	4	1	2	3	4	1	2	3	4	1	2	3
SO1	Design and manufacturing of photonic nanoestructures																											
SO2	Surface functionalization & charact.																											
SO3	Nanoparticles deposition & charact.																											
SO4	WERS setup assembly																											
SO5	Simulación of other potential structures for future work using CST																											
	Writing																											

Figure 1.2: Workload schedule.

In this work, gold-covered silicon disks have been used to functionalize with the BPT molecule. These disks would have been designed previously to the start of this project. Additionally, guided circuits functionalization has been carried out with the ABIZ molecule. Obtaining stable SAMs with

the ABIZ molecule is of special interest due to its outstanding response in the THz range. Three different types of structures were used in this work, which will be referenced in Chapter 3.

Materials, reagents and facilities used in this work were provided by the Nanophotonics Technology Center (NTC). As this work is a multidisciplinary project, other people have been involved in **SO1** and **SO5** objectives: PhD Javier Redolat Querol and Dr. Amadeu Griol Barrés collaborate in the design and manufacture of the substrates (**SO1**), respectively; Dr. Francisco Javier Diaz Fernandez and PhD student Evelyn Diaz Escobar were collaborating in the assembly and validation of the WERS were(**SO5**). Finally, this system will be part of a more complex device developed by one of my supervisrors Dr. Elena Pinilla Cienfuegos, included in her research project [1].

This project is part of the European THOR project (TeraHertz detection enabled by mOlecularR optomechanics[2]. THOR's main objective is the development of a new concept of signal up-conversion from far/mid-infrared (FIR/MIR or THz frequency band) to visible/near-infrared (VIS/NIR) radiation using molecular optomechanics. The final result of this project will be on-chip THz signal detectors that will able to offer a low cost-effectiveness ratio and operate in ambient temperature conditions. This project is carried out by a consortium constituted by the Universitat Politècnica de València and CSIC (Spain), AMOLF (The Netherlands), Imperial College London and University of Cambridge (UK), Ecole Polytechnique Federale de Lausanne (Switzerland) and Lytid Sas (France).

In addition, my work as a NTC researcher is supported by a collaboration grant, provided by the *Ministerio de Educación y Formación Profesional* (MEFP), hence I will be able to continue collaborating in this research after completing this project. For this reason, there is a Chapter entitled "Ongoing work" (see Chapter 5), which will mention the lines of research that will continue being investigated in the coming months.

[1] Grant No. SEJIGENT/2021/039

[2] H2020-FETOPEN-2018-2019-2020-01, EU. Term of completion: August 2022. Link: https://h2020thor.eu/.

Chapter 2

THEORETICAL BASIS

2.1 Raman Spectroscopy

Spectroscopy is the science that studies the interaction of electromagnetic radiation with matter. When light interacts with matter at molecular scale, various phenomena including elastic and inelastic scattering can result. Raman spectroscopy is based on the detection of the inelastic scattering by exposing a sample to a monochromatic beam at a certain wavelength λ_i, providing information on the interaction between the incident photon and matter [15]. The fundamental principles of Raman spectroscopy will be explained bellow, as it is of major relevance to have a general understanding of the technique in order to discuss the remaining chapters.

Since molecules are composed of different types of atoms carrying electrons and nuclei, vibrational motions depend on the chemical and physical nature of the bonds between them. The frequency and energy associated to vibrational motions is directly related to the type of binding [16]. Regarding light-molecule interaction, when light interacts with a molecule with an associated energy E_0 much higher than the energy difference between two vibrational/rotational levels of this energy, it generates a transient energy state commonly known as a *virtual state*. Being this an unstable state, the incident photons are rapidly scattered elastically or inelastically. Elastic scattering occurs when photons are scattered with an energy equal to the incidence energy. This is known as Rayleigh scattering, where $E_{Rayleigh} = E_0$. Alternatively, inelastic scattering occurs when the photon is scattered with an energy higher or lower than the incidence energy, known as Raman scattering, where $E_{Raman} = E_0 \pm E_{vm}$, where E_{vm} is the energy dependent on vibrational modes [15]. Only one in every $\approx 10^6$-10^8 photons is Raman scattered, which defines it as a weak process [17]. Figure 2.1 shows the scattering event.

Concerning inelastic scattering processes, molecular vibrational modes are the elementary excitations which determine whether the energy of the exit photon is lower or higher than the energy of the incident photon [18]. For this reason, Raman spectroscopy is also classified as a *Vibrational Spectroscopy* type [19].

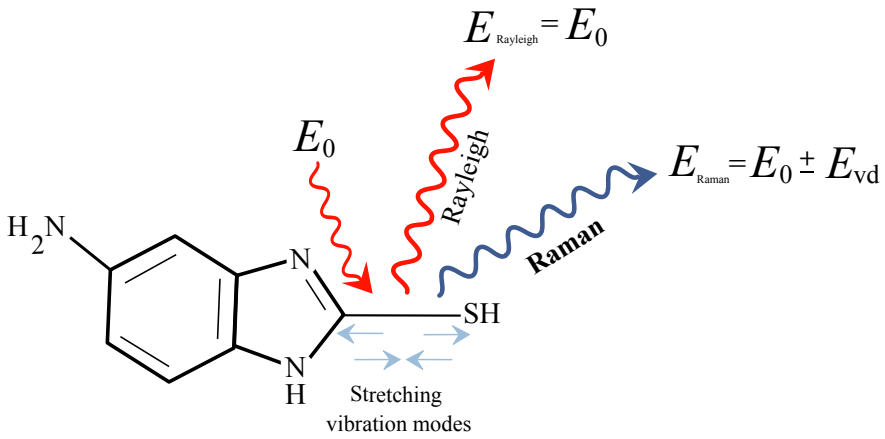

Figure 2.1: Schematic representation of the Rayleigh and Raman scattering events. E_0 is the incident energy of a photon. $E_{Rayleigh}$ corresponds to the Rayleigh scattered photon. E_{Raman} corresponds to the Raman scattered photon energy, whose value is equal to the energy of the incident photon coupled to a certain energy E_{vd} which depends on the mode of vibration of the ABIZ atoms. The sign of the energy coupling depends on the Stokes or Anti-Stokes scattering.

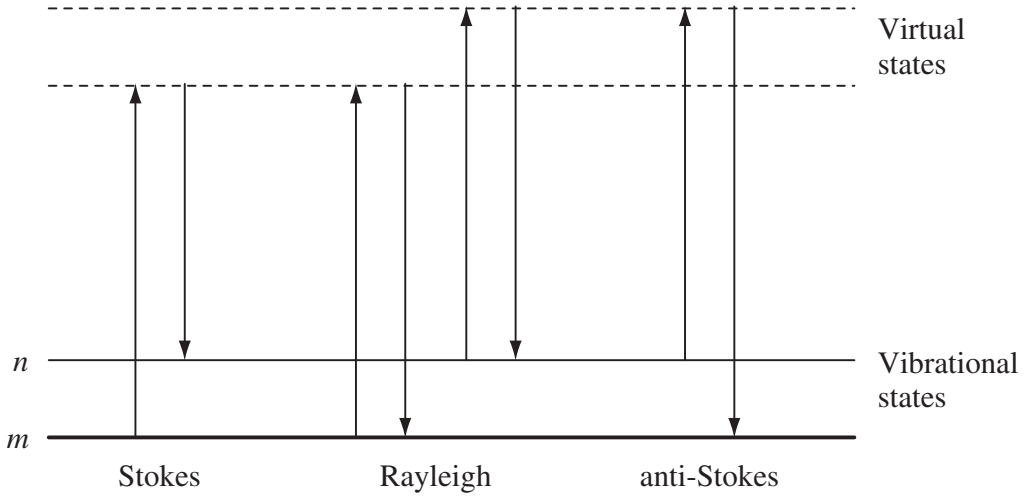

Figure 2.2: Diagram of Rayleigh and Raman scattering process. *m* is the lowest vibrational energy, while *n* corresponds to a higher vibrational state of energy. Low energy represented by upward arrows and scattered energy represented by downward arrows. Image extracted from [17].

Figure 2.2 shows the diagram of Rayleigh and Raman scattering process. The energy of the virtual states depends on the frequency of the light source used in Raman spectroscopy. When Rayleigh scattering takes place, the light returns to the same energy state as the molecule returns to its initial vibrational states. This is the the most frequent case, consequently the Rayleigh scattering signal is the strongest. Otherwise, if the Raman scattering starts from a particular vibrational state and the molecule absorbs energy, the final vibrational mode will be higher than the initial one. This is what is called Stokes. Consequently, the scattered photon has a lower energy associated with it, so its wavelength will be longer and its frequency lower. Alternatively, starting from a particular state, when the molecule release energy Anti-Stokes takes place and the final vibrational mode is lower than the initial one. Therefore, the photon is scattered with an associated shorter wavelength and higher frequency [17].

The energy of a photon depends on its frequency, according to:

$$E_0 = h\nu_0 \tag{2.1}$$

where h is the Plank constant and ν_0 is the frequency of the incident photon. As $\nu_0 = \frac{c}{\lambda_0}$, where c is the speed of light and λ_0 is the wavelength of the incident photon, $E_0 = \frac{hc}{\lambda_0}$. Nevertheless, in spectroscopy procedures, the wavenumber format is used since it interesting having a linear relationship with energy, being the wavenumber:

$$\upsilon = \frac{\nu_0}{c} = \frac{1}{\lambda} \tag{2.2}$$

Raman scattering is independent of the laser used, and therefore the Raman spectrum is represented as a shift of the inverse of the input wavelength with respect to the output wavelength of the photon, being the shift represented as a wavenumber [15]:

$$\upsilon = (\frac{1}{\lambda_0} - \frac{1}{\lambda_{Scattered}}) \times 10^7 = \frac{\nu_0 - \nu_r}{c} \tag{2.3}$$

Raman spectroscopy provides relevant information about chemical structure and spatial configuration, as well as the quantity of substrate. Figure 2.3 relates the Raman spectra to the properties of the substrate. This is particularly important as it allows both qualitative and quantitative characterization of samples using the same technique. For this main reason, it is typically said that Raman spectroscopy offers a *fingerprint* of a chemical specimen. In addition, Raman spectroscopy can be applied to both solid and solution samples, as well as to compounds derived from powders and surface films, without prior sample preparation [17].

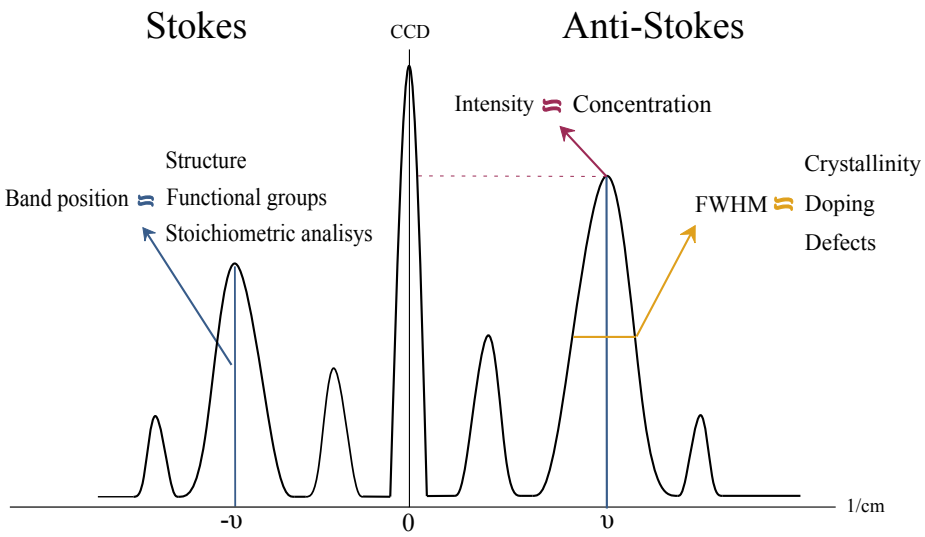

Figure 2.3: Information extracted from the Raman spectrum according to the measured parameters. Abscissa axis represents the shift between the incident photon and the scattered photon represented in wavenumber. Raman Strokes and Anti-Strokes are represented. The extremely high intensity at 0 is due to Rayleigh scattering, which intensity is mainly due to the elastic nature of most of the scattering produced. Occasionally, Stokes and Anti-Stokes are quasi-symmetric, which is not always the case.

The Raman phenomenon is of vital importance for the up-conversion to take place. The molecules that perform the coupling of signals must have a Raman spectrum of high intensities at THz. In this project, Raman instrumentation has been used only for characterization, but the latter should not be ignored. The Raman instrumentation used to characterise the samples in this project will be explained in Chapter 3.

2.2 Surface Enhanced Raman Spectroscopy (SERS)

Surface-Enhanced Raman Spectroscopy is widely used to achieve higher intensities in the Raman spectrum and be able to better identify the characteristics of surface adsorbed molecules, whose signal is challenging to detect as a result of its reduced thickness [20, 21]. Regarding molecular up-conversion, it is essential to boost the signal in order to have the greatest amount of information at the output of the system. In this work, SERS has been used to characterise the Self-Assembled Monolayers (SAMs), boosting their Raman characteristics. The enhancement phenomenon comes from different natures, which can be caused by electromagnetic enhancement (EM) or chemical enhancement (CHEM). In this work, EM has been used as it tends to result in higher boosted responses [19]. Therefore, it is necessary to briefly explain this phenomenon and the SERS mechanism used in this project.

2.2.1 SERS in plasmonic substrates

When laser light at a particular wavelength interacts with a metallic nanostructure, it occurs an optical event response known as Surface Plasmon Resonance (SPR). A SPR is an especial resonance, which consists on the oscillation of the conduction band electrons [22]. In gold, plasmon maximum peaks are observed in the visible region, being excited at optical frequencies [23]. Additionally, when a beam of light at a particular wavelength λ_p interacts with a NP whose size is NP_{size} nm, being $NP_{size} < \lambda_p$, it occurs what is known as Localized Surface Plasmonic Resonance (LSPR), phenomenon that generates a very high local E field confinement [24]. Figure 2.4 shows the E field confinement generated by LSPR.

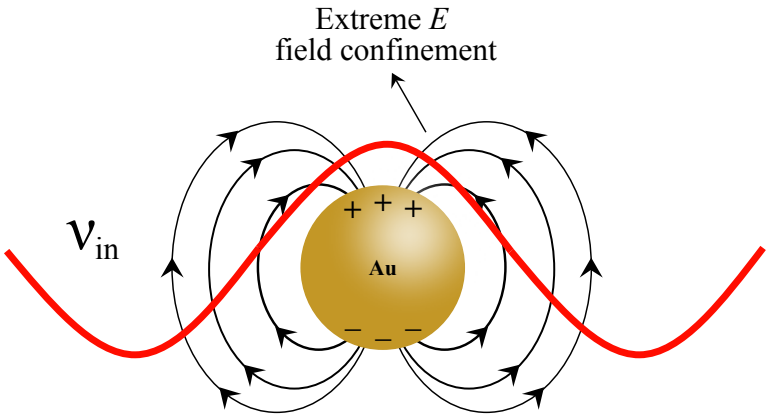

Figure 2.4: LSPR phenomenon. Interaction between a laser light, which frequency is ν_{in} Hz, and a gold NP which size is NP_{size} nm. It is noted that $NP_{size} < \lambda_i n = \frac{c}{\nu_{in}}$, being λ_{in} the laser light wavelength. At the NP surface, it can be seen the excitation of localized surface plasmon resonance and the resulting E extreme field confinement.

Electromagnetic enhancement especially occurs when the EM field is confined to a certain point of a structure where resonance behaviour exists. This occur naturally on metallic nanoestructures when its interaction with light generates the LSPR [25]. Additionally, inelastic scattering can also excite the LSPR, producing as a result the enhancement of the Raman signal. Figure 2.5 shows the enhancement of both elastic and inelastic Raman Anti-Stokes scattering as a result of the interaction with the LSPR-supporting nanoestructure. The resulting overall SERS intensity is given by:

$$I_{SERS} = I_{in}(\nu_{in})I_{in}(\nu_{in} + \nu_{shift}) = |E_{in}(\nu_{in})|^2|E_{in}(\nu_{in} + \nu_{shift})|^2) \tag{2.4}$$

where $I_{in}(\nu_{in})$ and $I_{in}(\nu_{in} + \nu_{shift})$ are the intensity of the incoming laser beam and the Anti-Stokes Raman scattering, respectively, and $E_{in}(\nu_{in})$ and $E_{in}(\nu_{in} + \nu_{shift})$ are the incident electric fields. Both intensity and electric field depends on the frequencies ν_{in} and ν_{shift}. When $I_{in}(\nu_{in})$ and $I_{in}(\nu_{in} + \nu_{shift})$ are of the same order of magnitude, the SERS intensity can be given by: $I_{SERS} \approx |E(\nu_{in})|^4$. It can be noticed that very high local electric fields E_{local} caused by LSPR generate a large Raman signal enhancement. In [23] an example is shown of how a local field E_{local}, a couple of

orders larger than the field associated with a given laser light E_{in}, can cause an increase in the Raman signal by 10^8 orders. Being $E_{local}/E_{in} = 10^2$, then the enhancement factor (EF) is:

$$EF = (E_{local}/E_{in})^4 = (10^2)^4 = 10^8 \tag{2.5}$$

In addition, the SERS intensity is dependent on the distance to the plasmonic surface according to $I_{SERS} \propto r^{-12}$, being r the distance to the surface, which makes SERS strongly surface dependent [23]. As Raman scattering depends on the vibrational modes of the molecule [26, 27, 28], the orientation of the molecules will also influence which vibrational modes are more enhanced. This, as will be discussed later, creates the need to produce properly assembled SAMs in order to enhance the vibrational modes of interest.

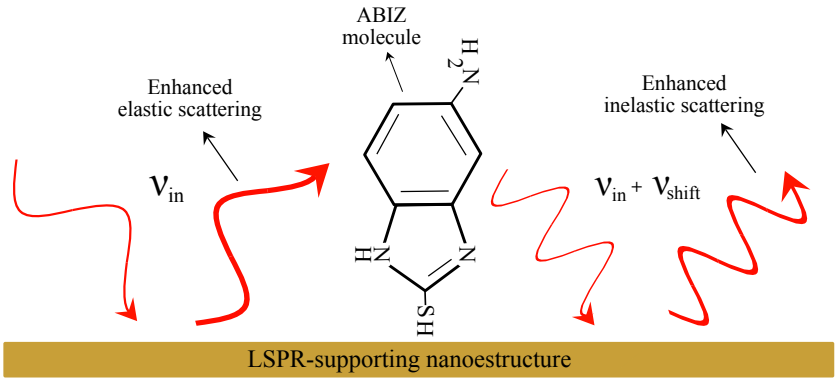

Figure 2.5: Interaction between a laser light, which frequency is ν_{in} and Raman Anti-Stokes scattering with $\nu_{in} + \nu_{shift}$ frequency with a LSPR-suporting nanoestructure.

Using these metallic NPs and LSPR-nanostructures has been proof an exceptional technique to amplify Raman signal [29, 30]. Additionally, SERS effectiveness strongly depends on the nanoestructures size and shape [31], making these properties an important design constraint. One of the state-of-the-art designs is the Nanoparticle on Mirror (NPoM) structure, which is described below.

NPoM structure

NPoM is one of the most robust example of SERS plasmonic nanostructure [32]. One of the advantages of NPoM configuration is that allows top-down manufacturing of the structures [33], simplifying fabrication processes. In this type of nanocavity, a NP is separated from an underlying metal film by a molecular monolayer [34] or by a thin dielectric film [35]. The space between the NP and the mirror (metallic surface) is called a *hot-spot*, due to the EM field enhancement caused by the hybridation between LSPR of the metallic NP and the propagating SPR of the metallic surface [36]. Additionally, if the space between the NP and the metallic surface is bridged by bonding molecules, the SERS phenomenon created by the EM enhancement allows the detection of the molecules within the *hot-spot* space [37].

In this work, the NPoM configurations are given by gold NPs and a metallic gold surface. The space between the NP and the mirror is provided by the SAM molecule, which can be either BPT or ABIZ, as will be explained in Chapter 3. Creating the gap or *hotspot* by using molecules allows their Raman signal to be amplified by SERS, as mentioned above. Figure 2.6 shows the schematic NPoM configuration used in this work. As can be seen, the ABIZ Raman scattering is enhanced by SERS created within the NP and the mirror. This is of particular interest, as this configuration allows integrated circuits which ensure the enhancement of the molecular response.

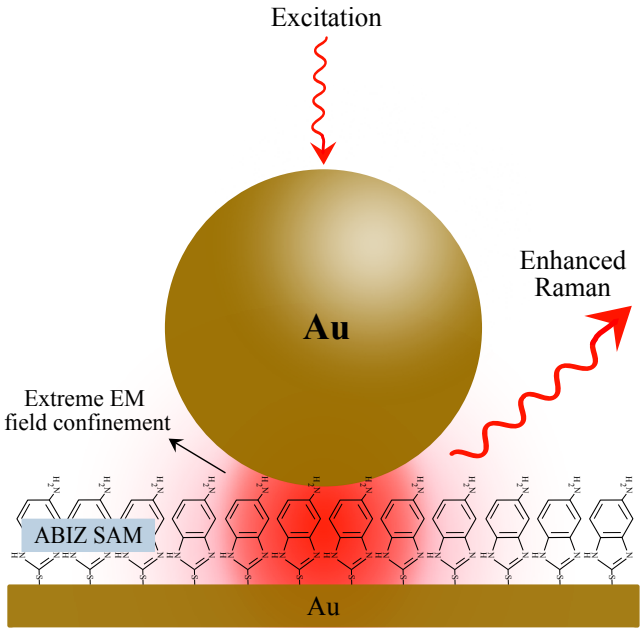

Figure 2.6: SERS in NPoM structure. The Au NP is linked to a gold surface by ABIZ molecules. Input and output beams oscillation are not scaled with the size of the NP, as the size of the NP must be shorter than the light beam wavelength.

It should not be forgotten that both BPT and ABIZ molecules are responsible for triggering the up-conversion, so the visible/Raman signal that will be enhanced is the one coupled to the THz. The following section will delve more deeply into the molecular optomechanical behaviour that enables the coupling of the signals.

2.3 Signal up-conversion through molecular optomechanics

Optomechanics is the application of laser light in order to control mechanical vibrations [38]. Recently, optomechanical cavities have been proved useful in terms of sensing and signal up-conversion [39, 40, 41]. The Fabry-Pérot resonator is the conventional structure to explain optomechanical cavities. In this type of cavity, consisting in two parallel mirrors, the light field E is forced to bounce between them, as one of them is mobile due to its connection to a dock [42]. The reflection in a Fabry-Pérot cavity generates the momentum transfer of photons, which describes the radiation pressure coupling that is given by [43]:

$$|\Delta p| = \frac{2 \times h}{\lambda} \tag{2.6}$$

where $|\Delta p|$ is the momentum transfer of a single photon, h is Plank's constant and λ is the photon wavelength.

The radiation pressure forces produced by the photons that have been confined generates the activation of the cavity mechanical modes [44]. Studies have shown that the optomechanical cavity signal controlled by plasmonic modes can be coupled to molecular vibrational activity [45, 41]. Regarding this molecular optomechanics approach, optomechanical transduction with molecules has been studied recently and presents a promising future in signals up-conversion between 5 and 50 THz into the visible, since natural oscillation frequencies are resonant with the incoming field [46], being the incoming field generated by the incidence of a visible laser on the plasmonic cavity. In order to understand signal up-conversion lead by molecular optomechanics, the interaction between molecular vibrations, IR EM field E_{IR} and visible (or pump laser) EM field E_p needs to be considered. Note that, for simplicity reasons, in this work IR references Far-Infrared (FIR) and Mid-Infrared (MIR). Near-infrared (NIR) is sufficiently close to the visible that it can even be used as a pump.

Figure 2.7 shows the differences in the Raman spectrum regarding an optomechanical structure. The structure selected to represent the example is NPoM, since all the work is focused on this, but it could have been any other plasmonic configuration that allows SERS and signal coupling. In Figure 2.7.a), only the pump laser is incident on the optomechanical structure at a certain frequency that excites the vibrational modes of the molecule at THz. The output represented is the Anti-Stokes Raman scattering, with a wavenumber of 333.33 cm or 10 THz, as shown in Figure 2.7.c). On the other hand, in Figure 2.7.b) the cavity is also incident with a signal in the IR with a frequency of 10THz. As can be seen in Figure 2.7.b) and 2.7.c, the output of the system will now be the THz signal coupled to the Anti-Stokes signal of the molecule corresponding to the same vibrational modes, which provides an increase in intensity in the Raman spectrum at that frequency.

Molecules must present activity at both visible (Raman) and IR (THz) frequencies in order to perform optomechanical molecular coupling. Therefore it is of great interest to select and study such molecules. An European research consortium has developed software that provides information on 2800 molecules that exhibit this expected responses [47], including BPT and ABIZ. Figure 2.8 shows the IR, Raman and upconversion spectrum from the two molecules. As can be seen, ABIZ presents higher up-conversion. Additionally, ABIZ up-conversion is produced at frequency ranges which are of higher interest, since lower wavenumbers correspond to lower THz frequencies. For consideration, the gap from 0.1 to 30 THz corresponds to wavenumbers from 3.33 cm^{-1} to 1000 cm^{-1}, being more interesting the range nearer to 0.1 THz. Behind the latter lies the importance of creating new SAMs with ABIZ molecules, which provide more efficient results. This software it has been used in Chapter 4 to verify the functionalisation of SAMs with ABIZ.

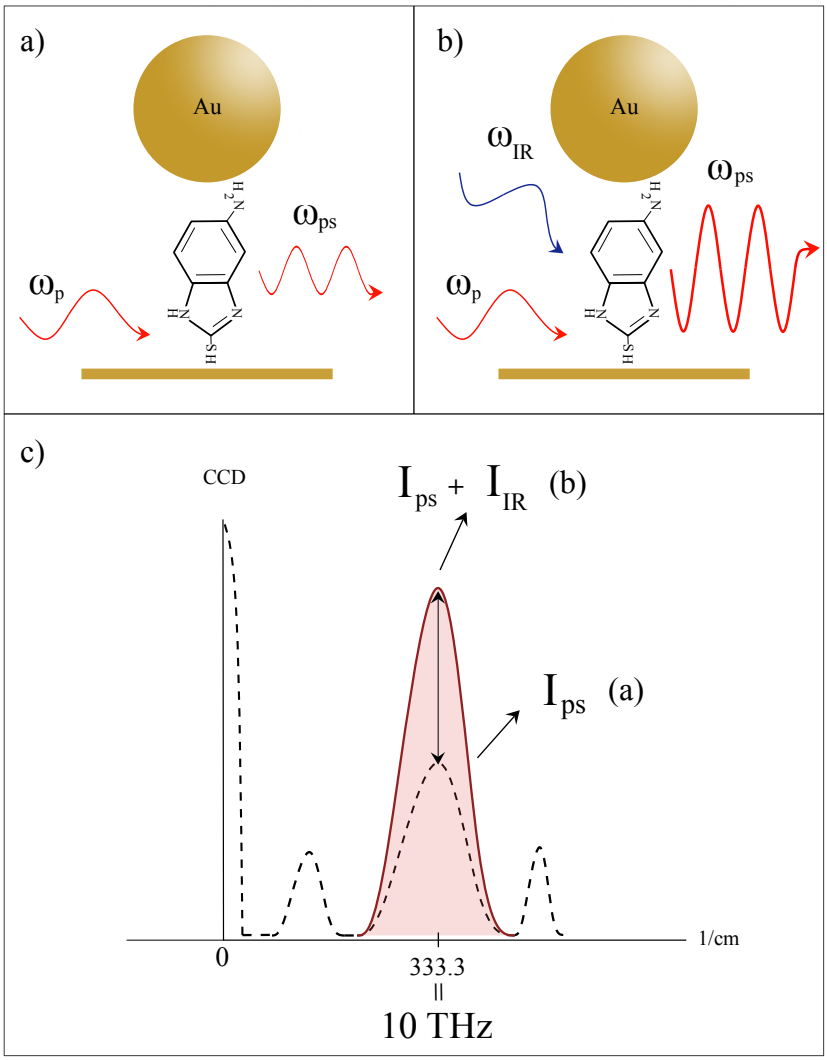

Figure 2.7: Example of a nanophotonic device based in NPoM for up-conversion (schematic). ABIZ is the molecule with THz response, responsible for performing up-conversion. a) ω_p references to visible (or pump laser) EM field, while ω_{ps} is the Raman Anti-Stokes scattering, whose wavenumber ν = 333.3 cm^{-1} = 10 THz. b) ω_{IR} is the IR EM field, which frequency is 10 THz. The output intensity signal is $I_{ps} + I_{IR}$, and its frequency corresponds to the Anti-Stokes scattering with 10 THz shif, but with the intensity higher as a result of the signals coupling. c) Representation of the Raman spectrum in both cases. I_{ps} is the Raman intensity associated with the visible pump, while I_{IR} is the intensity associated to the THz beam. One can notice that in case a) the signal at 10 THz is much lower than in case b), as in the latter the coupling of the signals generates an increase of the Raman signal at the vibrational frequency of the molecular mode which coincides with the frequency of the wave at THz. For simplicity, only the Anti-Stokes Raman scattering is represented.

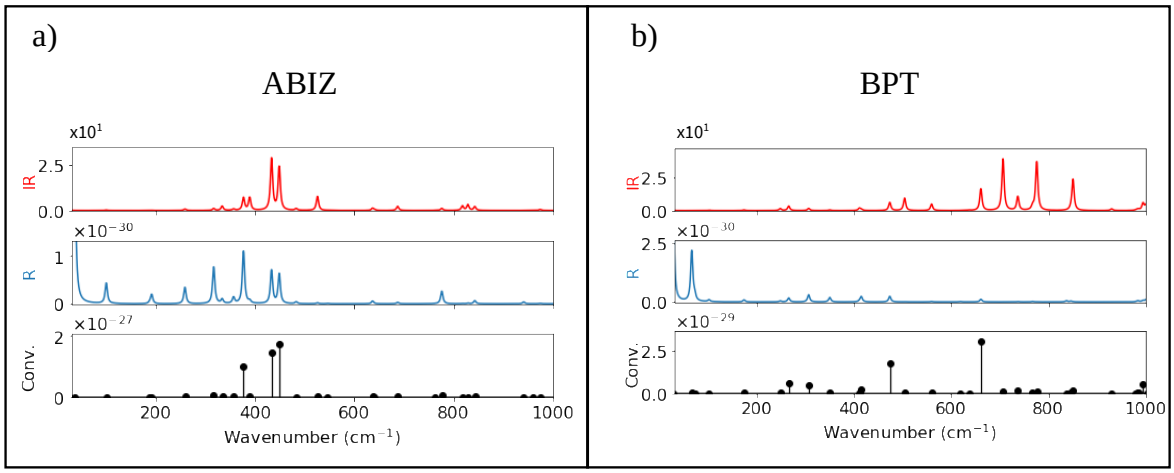

Figure 2.8: THz, Raman and up-conversion responses from BPT and ABIZ molecules. Graphics extracted from online platform *Molecular Vibration Explorer* [47].

2.4 Wave-guided Enhanced Raman Spectroscopy (WERS)

Wave-guided Enhanced Raman Spectroscopy (WERS) offers an alternative to conventional SERS. The potential application of WERS is essentially the same as of SERS, as both are methodologies used to enhance the Raman signal. In order to enhance the inelastic scattering, dielectric waveguides are used to generate a strong evanescent field, through which laser light interacts with the structures residing on the surface of the waveguide [48]. WERS has proven to be useful sensing analytes localised on the surface of dielectric material guides, showing significantly reduced noise comparing to conventional Raman signals as a result of the interference reduction, which is intrinsic to the evanescent excitation and collection of Raman emission in waveguides [49]. Additionally, WERS allows the structures to be integrated on chips, which is especially important. WERS still a technique under development, and the studies mentioned above base this phenomenon on liquid samples.

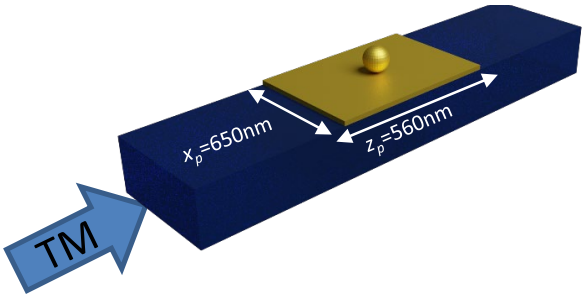

Figure 2.9: WERS structure used in this project. The structure is used to perform the wave-guiding process in TM polarisation (the electric field is polarised parallel to the plane of incidence). The plasmonic structure on the surface of the silicon nitrure guide corresponds to an NPoM, where both NP and mirror are gold. Image source: THOR's project.

Alternatively, if a plasmonic structure is placed on the surface of the dielectric guide, the evanescent field causes excitation of the SPR and of the LSPR if it is an NP. In this work, silicon nitride waveguides with a gold patch on top have been characterised (see Chapter 4, Section 2). A SAM has been generated on the gold patch to place an NP on top of the patch, thus creating an NPoM structure on a waveguide. Simulations have been performed and it has been observed that the waveguide can excite the plasmonic cavity functionalised with ABIZ, which is responsible for signal coupling. In addition, by introducing the pump signal (visible range signal), the waveguide can also collect the Raman signal of the molecular vibrations in the THz coupled to the signal in the IR. Figure 2.9 shows the schematic one of the possibles structures that allow WERS. Simulations of other possible configurations have been performed (see Chapter 4, Section 5).

In this work, the structure that allows WERS combined has been considered as it allows guiding the signal, which is extremely necessary for its integration in chips. Additionally, this type of configuration also works efficiently for characterising molecules. Therefore, it can also be used to characterise SAMs. To properly excite the system, this type of configuration requires a special Raman system that allows Raman guided configuration to be performed and collected, a system capable of measuring in guidance has also been assembled in this work. A WERS combined with SNOM setup has been assembled as part of this work. Due to time constraints, the system has been assembled but not optimised, being part of ongoing work (see Chapter 4, section 4).

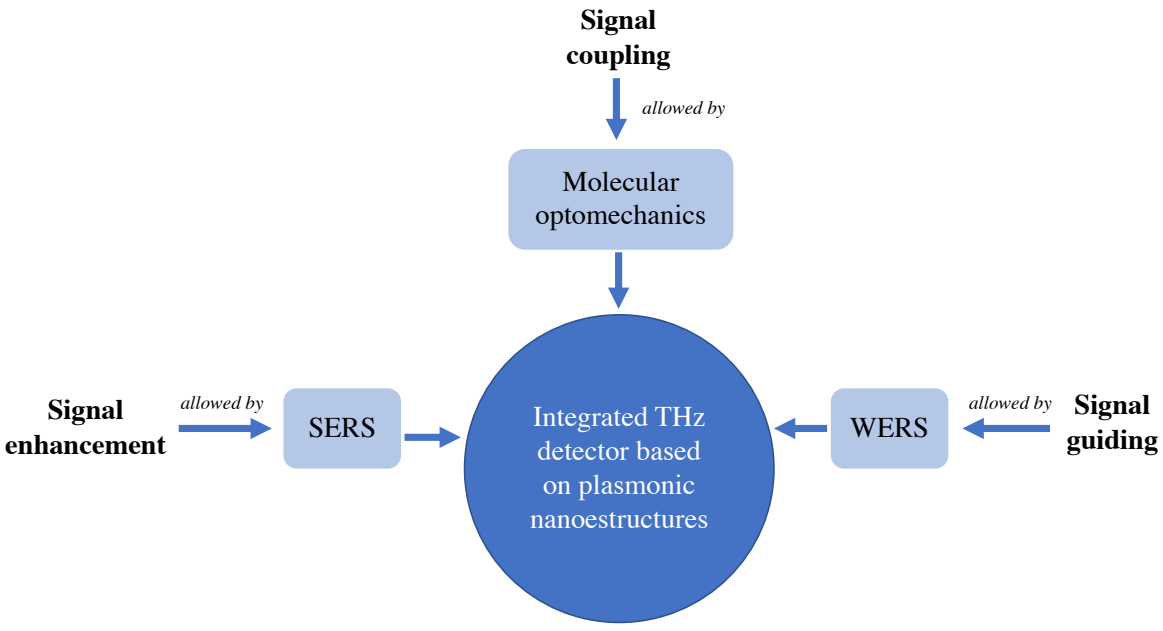

Figure 2.10: General overview of the phenomena to be considered for the development of THz detectors based on molecular conversion and plasmonic structures. The following points should be recalled: in this work SERS is realised by the NPoM structure; the molecular optomechanics of interest is that related to ABIZ and BPT molecules which have molecular vibrations at THz; WERS setup will be assembled from scratch.

Chapter 3

MATERIALS AND METHODOLOGY

3.1 Fabrication of photonic nanostructures

The aim of this section is to describe the design and manufacturing processes involved in the fabrication of the different lithographed samples used in this work. It is worth noting that this first Section 3.1, and the results shown in Section 4.1, can be considered as the basis of this SAMs characterization study.

3.1.1 Theoretical design using CST

In order to ensure that the lithographed structures will exhibit the expected performance, it is necessary to make a first approximation based on simulations. The simulations performed for the design of the structures used in this work were created using CST STUDIO SUITE software. These simulations were performed in collaboration with researchers from *Universidad Católica San Antonio de Murcia* (UCAM) and NTC. Some of the results obtained in these simulations are shown in Section 4.1.

3.1.2 Technological manufacturing process

In this study, three different types of lithographed samples have been used: gold disks on; silicon nitride (SiN) guides with a gold patch on the guide surface; orthogonal (SiN) guides with a gold patch on the orthogonal junction. These structures are lithographed over silicon (Si) wafers, and will be illustrated throughout the chapter. The lithography process refers to the nano-printing of the mentioned structures. The responsable for the nano-manufacture is Dr. Amadeu Griol , who was in charge of handling the necessary machinery for lithography. The same nanofabrication procedure has been used for the manufacturing of the three sample, which includes a sequence of different steps [50], which are explained below and schematically represented in Figure 3.1.

- **Wafer cleaning.** A silicon wafer is used as base of lithographed structures, which must be properly cleaned. Cleaning with IPA (Isopropyl Alcohol) and Acetone using the *Coater EVG 101* device is the first step, which followed by an oxygen plasma treatment at 400W, for a period of up to 10 minutes using the *Tepla PVA* machine.

- **Spin Coating: resist deposition.** *Coater EVG 101* is used in this step. The Spin Coating technique provides a homogeneous surface of a photoresist. Two types of resists can be used: in case of using positive resist, the exposed areas will disappear with the subsequent development step. Alternatively, if negative resist is used, the exposed areas will remain. Here, PMMA positive resist is used, as it allows smaller designs to be produced with higher quality.
- **Curing.** The *Brewer Model 100CB* device separates the solvent from the photoresist, in order to improve the resist adhesion.
- **Exposition.** Although there are different methods in order to perform the resist exposition, here electron beam lithography is used. The resist is irradiated by a focused beam of electrons, performed by *Raith 150* device. As the resist used here is positive, the mask used must provide the target circuit.
- **Revealing.** Removal of the photoresist which is not part of the mask, using *Brewer 100CB* device.
- **Attacking.** Removal of silicon nitrure or gold not protected by the mask, using *RIEICP* (Reactive Ion Etching with Inductived Coupling Plasma Source).
- **Resist elimination.** Mask removal.

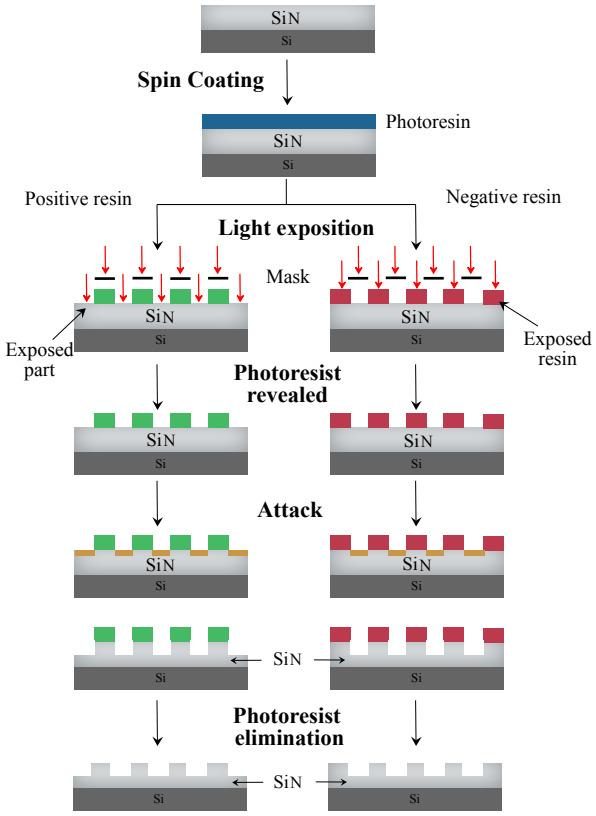

Figure 3.1: Nanofabrication process. Image adapted from [50].

Figure 3.1 process refers to the guides samples, as it is lithographed on SiN. In order to obtain to obtain the gold disks, the above procedure is applied to a layer of gold placed on top of the Si. In addition, for the latter two structures, it is necessary to add an extra step:

- **Gold patch placement.** Add the gold patch to the samples surface using evaporating techniques.

3.2 Elaboration of Self-Assembled Monolayers (SAM)

As previously stated, two different types of molecule have been used to perform the funcionalization of plasmonic surfaces. The molecules purchase reference and the structures functionalized with each molecule are bellow:

- **BPT:** Purchased from *Merck-Sigma Aldrich*, reference product: *752207-1G*, package size: *1g*, *97*%, state *solid*. Functionalized structure:
  - Gold disks.
- **ABIZ:** It should be noted that there are scarcely previous studies on SAMs using ABIZ, so this work presents a new method for functionalising plasmonic surfaces with this molecule. Purchased from *Merck-Sigma Aldrich*, reference product: *536067-25G*, package size: *25g*, test *99*%, state *solid*. Functionalized structures:
  - Three SiO2 samples with surface evaporated gold for SAM verification.
  - Gold patch at individual SiN wave-guides surface.
  - Orthogonal SiN wave-guides with a gold patch at the junction of both guides.

3.2.1 Cleaning of substrates

The distance between the NP and the gold surface determines the confinement of the EM field, so that shorter distances result in greater confinement. It is therefore important to obtain one molecule thick SAMs, for what it is essential to ensure the maximum stability of the chemical reaction environment. Hence, an appropiate cleaning of both the substrates and the vessels is required.

Vessel cleaning

Vessel cleaning was performed using a chemical method commonly known as *piranha*. Two beakers, gloves, an ultrasonic cleaner, absolute ethanol, sulphuric acid (H_2SO_4), hydrogen peroxide (H_2O_2) and Milli-Q water were needed. This cleaning process was triggered by combining H_2SO_4 with H_2O_2 (50/50), resulting in an exothermic reaction. The reaction is left to react for three minutes. Subsequently, the residues are drained and the vessel is sonicated with Milli-Q water for five minutes. Finally, ethanol is used to dry the inside of the vessel.

Substrates cleaning

There are several physical methods of substrate cleaning, including plasma, UV and ozone treatment. Alternatively, in this work a chemical method known as *soft piranha* has been used. For this, two beakers, gloves, an ultrasonic cleaner, absolute ethanol, ammonia NH_3, hydrogen peroxide H_2O_2 and Milli-Q water were needed. The process was performed in the Biophotonics laboratory of the NTC, inside a fume extractor hood. *Soft piranha* results from combining NH_3 and H_2O_2 with Milli-Q H_2O, being the stoichiometric (1:1:2). Substrates were cleaned by three 5 min sonication cycles in diluted basic piranha solution (or *soft piranha*): NH4OH(conc.): H2O2:H2O, 1:1:2 (v/v/v). Between each sonication cycle the substrates were immersed in a fresh aliquot of piranha solution. The substrates were finally washed by sonication in ultrapure Milli-Q water during 5 min. Finally the substrates were thoroughly blow dried before used. Ultrasonic cleaner: IBX ultrasonic cleaner (power 120 W) was used.

3.2.2 SAM with BPT

As previously stated, BPT is a widely used molecule for creating SAMs [51, 52] as physical processes are not required, simplifying functionalization process to a simple, chemical process for which no sophisticated instrumentation is required. Considering cation BPT molecular formula, $C_{12}H_9S^-$, and molecular weight, 185.27 g/mol [53]. I this study, the BPT functionalizing method performed in [13] was used. For this, three beakers, gloves, an ultrasonic cleaner, a pipette, cling film, absolute ethanol, BPT and isopropanol (IPA) were needed. The following steps were required, orderly:

- Dump 40 ml ethanol in a beaker using a pipette.
- Place cling film on the scale and pour in BPT (solid) to 7.7 mg.
- Pour the BPT over the 40 ml ethanol and mix softly, creating a 1mM BPT-ethanol solution.
- Immerse the sample into the solution, ensuring to place the lithographic surface facing upwards.
- Leave immersed for 12 hours.
- Extract sample and pour isopropanol (IPA) to the surface, followed by drying with N_2.

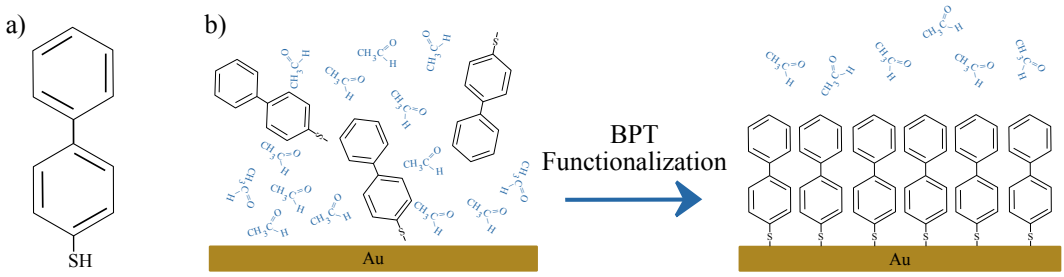

Figure 3.2: a) BPT 2D structure. b) Gold surface functionalization using BPT.

As can be seen in Figure 3.2.a, BPT is composed by two aromatic rings and one thiol. It has no other functional groups, so it is a remarkably stable molecule, usually providing cohesive SAMs. Figure 3.2 shows the BPT functionalization process, activated by ethanol.

3.2.3 SAM with ABIZ

Alternatively to BPT, ABIZ shows a structure consisting of a benzene with an amine, a pyran with two nitrogens and a thiol, creating a less stable structure than BPT. Figure 3.3 shows ABIZ structure, being its molecular formula $C_7H_7N_3S$, and molecular weight 165.22 g/mol [54]. In order to perform SAMs using ABIZ molecules, two beakers, gloves, absolute ethanol, cling film, an ultrasonic cleaner, a pipette and ABIZ molecules were needed. In addition, three non-lithographed Si-gold evaporated samples were used for SAMs verification. Lithographed samples were functionalized after testing the viability of the method. See Chapter 4, Section 3 for recipe and characterization results.

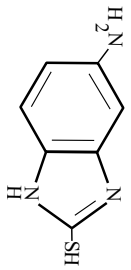

Figure 3.3: ABIZ schematic 2D structure.

3.2.4 Protonation using HCl

Protonation is a technique which harnesses the property of certain molecules to become positively charged. In this case, ABIZ molecule has an amine group NH_2, which can be eventually become NH_3^+. This method consists on combining a strong acid such as hydrochloric acid (HCl) with Milli-Q water. For this, a beaker, gloves and a pipette is needed. This method has been used in orthogonal wave-guides lithographed samples and in one of the non-lithographed samples. See Chapter 4 for results.

3.3 Deposition of plasmonic nanoparticles

Desposition of plasmonic NPs is required for both verify the SAMs coherent formation and for the SERS phenomenon to be produced by SPoM structure. The SERS phenomenon allows BPT and ABIZ monolayers to be detected, hence SAMs to be characterized. However, the placement of the NPs in the desired areas is a challenging task, due to the small dimensions of both the lithographed samples and the NPs. For this study, two types of Accurate™ Spherical Gold Nanoparticles of different sizes, 60 nm and 150 nm, were supplied by Nanopartz™. As can be seen in Figure 3.4, the right vessel contains 150 nm NPs and the left one contains 60 nm NPs. It can be noticed that, despite

having the same concentrations, the size of the NPs causes the light to diffract differently in each solution.

Figure 3.4: Negatively charged 60 and 150 nm gold NPs.

3.3.1 Drop-casting technique

Conventional method of gold NPs deposition consist on release a drop of the solution containing the NPs onto the surface samples. For this aim, a 20-200 µl micropipette, NPs solution, Milli-Q water and N_2 are necessaries. This method works properly for non-lithographed samples. Conversely, NPs often do not settle where they should, hence new NPs deposition techniques have to be developed.

3.3.2 Micro-contact printing

Micro-contact printing, which is a novel technique under development, comes up from the need to place NPs accurately. For this technique, a polydimethylsiloxane (PDMS) stamp is generated using a Si lithographed master. The PDMS is synthesized in the laboratory each time a new stamp is required. PDMS stamps manufacturing is performed employing the "Kit Silicon Elastomer Sylgard 184", and it requires several steps. The master is elaborated in the NTC's nanofabrication clean room. In addition, IPA, N_2, a disposable glass, curling agent, base,an ultrasonic cleaner, a micro-scale, a vessel and an oven are materials needed. See Chapter 4 Section 2 for recipe and results provided by the implementation of this new methodology.

3.4 Characterization techniques used in this work

Raman spectroscopy. In order to acquire Raman spectra of the samples, the spectrometer *alpha300 RA* (Raman-AFM) from *WITec* has been used. This equipment provides information about the Anti-Stokes Raman scattering, and for wavenumbers below 80 cm^{-1} it can provide no information. Initially the laser incorporated in the machine is a monochromatic 532 nm (green) laser, but recently a monochromatic 633 nm (red) laser has been added; measurements could be made with both of them. The power of both lasers can be tuned, from 0.1 mW to 26 mW, and it has integrated an optical microscope, which allows the samples to be properly placed. Additionally, this equipment comes with an specific software which allows the user to define the measurement conditions.

Optical Microscope (OM). As mentioned above, *the Zeiss* optical microscope is integrated in the *alpha300 RA* (Raman-AFM) equipment. The embedded lenses are 10x, 20x, two of 50x and 100x.

Dark-field Optical Microscope (DFOM). This technique is performed focusing the light in the far field and transversely on the sample, obtaining negative OM images. A high-power spotlight is focused transversely and images are collected with the OM described above.

Atomic Force Microscopy (AFM). AFM is also incorporated at the Raman spectroscopy equipment. The mode of operation can be selected using the software. This is used for acquiring information about the Z axis of the sample, as the heights of the sample structures are measured using the AFM Tapping Mode. In this mode of operation, the probe vibrates at its natural frequency, which generates an intermittent contact with the sample surface. The variation on the frequencies are due to the to probe-to-surface distances.

Contact angle. Advancing and receding water contact angle measurements were performed by the "add and remove volume" method in a *Ramé-hart Model 90 Standard* Goniometer with Dropimage Standard software, equipped with an automated dispensing system. This device includes software as well as a fiber optic illuminator, 3-axis leveling stage, high-speed F4 Series digital camera, microsyringe fixture and assembly for manual dispensing. The system is improved with an automated dispensing system and manual tilting base.

Scanning Electron Mycroscopy (SEM). The *Zeiss Gemini 500* uses an electron beam and through *Raith 150* device creates 3D images. This is a strong visual technique, which allows the user to acquire high resolution, 3D nano-scale images.

Dynamic Light Scattering (DLS). Is a NPs characterization technique, which allows to acquire measurements as the charge of the NPs and their average size, as the gold NPs are in suspension. DLS measures the diffusion of particles moving under Brownian motion. The device used for this analysis was from *icmol*, and it is named *Malvern Nano Zetasizer*.

3.5 WERS setup assembly

Here, a new WERS setup will be assembled, in which no liquid sample will be required to perform. This work presents the first WERS setup combined with SNOM specifically designed to characterize guided circuits. For this, an Cr and Au alloy tip, 3D designed parts, two 3D stages, optic fiber, light sensors, a $1250-1550\ cm^{-1}$ laser, an USB camera, an objective and a microscope were needed. In addition, lithoraphed guide samples were required to be manufactured for verify the WERS setup. See Chapter 4, Section 4 for results.

3.6 Other potential circuits simulations using CST

In order to complete this work, it was considered appropriate to perform other potential simulations using CST that could be used for future photonic circuits to be lithographed. The results of this new simulations can also be used to characterize the influence of SAMS on photonic nanoestructures.

Chapter 4

RESULTS AND DISCUSSION

4.1 Simulations results

After learning how to operate CST, a simulation was performed to observe the influence of the SAM thickness on the signal collection process. The graphics shown in Figure 4.1 were conducted to check the correct operation of the simulations explained in Section 4.5. However, as this is a routine procedure in simulations to verify a correct design, it has been considered convenient to report it in this section. Figure 4.1 shows the comparison of the EM field enhancement results performed by three different SAM sizes (1nm, 1.5nm and 2nm high). The abscissa axis is the frequency of the wave, while the ordinate axis shows the electric field strength. As expected, thinner SAM thicknesses generate smaller distances between the NP and the gold surface, which consequently results in a higher confinement of the EM field. Typically, 1nm SAM is used in simulations.

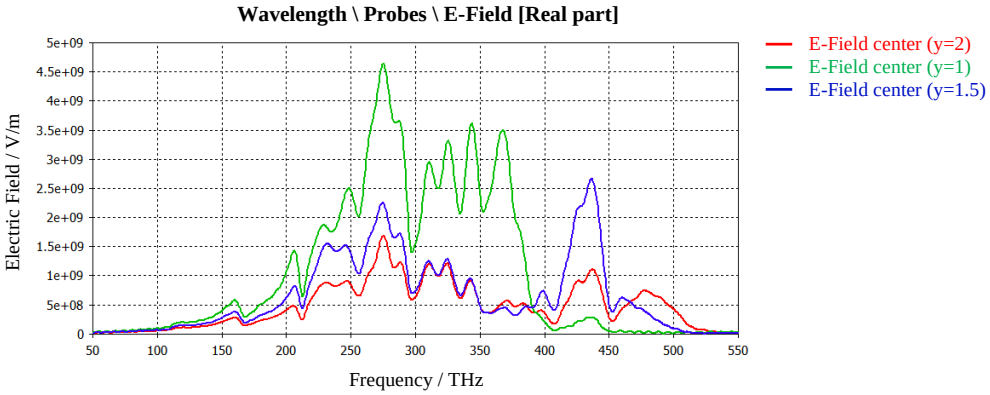

Figure 4.1: SAM thickness effect: comparasion between three thickness. *geom_sam_y* refers to the SAM thickness. The red curve is associated with the higher SAM thickness, which is 2 nm; the green one is associated with the lower, which is 1 nm; the blue one is associated with the 1.5 nm high SAM.

Simulations of the functionalized photonic structures used in this work can be considered the basis of this work, as their study has allowed the subsequent lithography of the circuits. Therefore, it has been considered necessary to briefly explain at least one of them. Simulations of the wave-guide and gold patch structure, which allow the study of the structure optical response of nanostructures, were

performed in collaboration with the PhD student Javier Redolat Querol.

Understandably, the maximum possible field confinement between the NP and the gold surface is determined by structures dimensions. Figure 4.2 shows the results extracted from the collection modes of the simulation performed for the study of the viability of the SiN guide with the gold patch at the surface. It shows the ZY plane, corresponding to the longitudinal section of the SiN guide and the gold NP, where the optical effect of the signal on the structure can be observed. The SAM has been simulated introducing a 1 nm thick dielectric material between the NP and the gold surface. SAM's width corresponds to the width of the guide, and is 100 nm long. The structure is excited with a 532 nm laser light, and the polarization of the EM field is TM, in order to have the electrical field paralleled to the input surface. The SiN guide is 3000 nm long, 200 nm high and 600 nm wide. The gold NP size is 80 nm. As can be seen in shades of green, the field around the NP is excited. In addition, an intense red colour can be observed in the gap between the NP and the gold surface, which represents an extreme confinement of the EM field. These design dimensions provide the expected and required response of the system, and where the ones used for lithography.

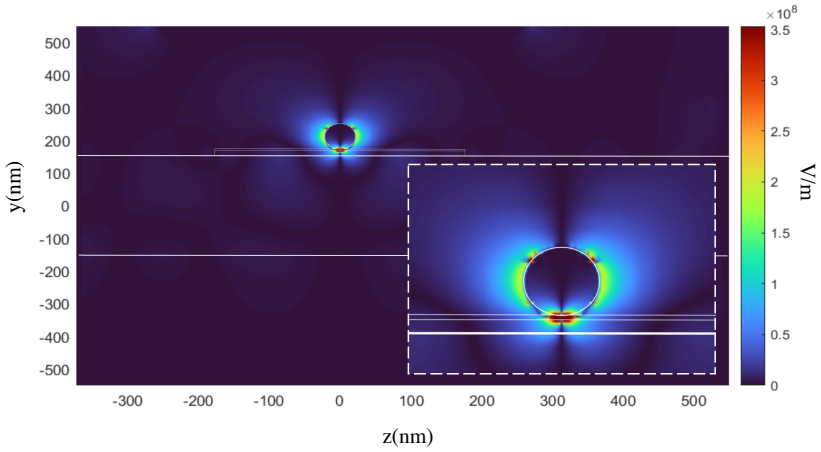

Figure 4.2: Gold patch CST simulation, collection excitation modes.

As this study is part of the European THOR project, several researchers were also involved in the structures simulation. The gold disks simulations were performed in collaboration with UCAM researchers, specialised in NPoM structures. However, this design is not useful for integrating circuits on chips, as they do not allow waveguiding. Orthogonal SiN guides simulations were performed by Enrique Vázquez, NTC researcher, and shown properly performance at visible wavelength.

4.2 BPT SAM characterization

BPT functionalisation technique is a widely used method and the results it provides are stable. Here, its characterization has been limited to contact angle techniques, and other visual techniques such as OM, AFM and SEM. In addition, the results of the new micro-contact printing NPs deposition technique will be studied in this section, which are also an evidence of a proper functionalization. As mentioned in Chaper 3, samples with gold disks litographed has been used to characterize the

SAM with BPT. Figure 4.3.a shows an OM image from the sample, where the gold disks can be seen. Alternatively, Figure 4.3.b shows an schematic, where disks dimensions can be seen. The disks are distributed in four 50 µm disks arrays. Disks dimensions are 233 nm high and 6 µm ∅.

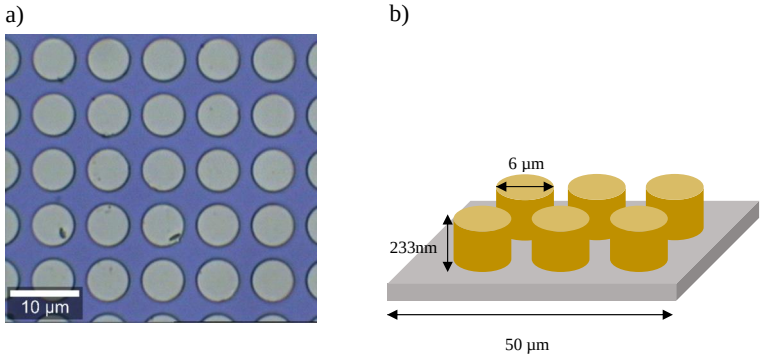

Figure 4.3: Gold disks lithographed sample. a) OM image before funtionalization. b) Schematic.

Before performing the gold NPs deposition, contact angle measurements where carried out before and after BPT functionalization. For this, the goniometer described in Chapter 3 was used. The advancing and receding contact angles are shown in Figure 4.4. Between each measurement, 1 µl was collected or released. The graphic shows the results measuring three times ten advancing angles and ten receding angles. Orange graphic corresponds to the BPT functionalized sample measurements, while blue graphic corresponds to the measurements before functionalization. As can be seen, after the functionalization with BPT, the contact angle increases between 10º and 15º comparing with the non-functionalized measurements. Considering a coherent funciontalization, this was to be expected, as BPT molecule is more hidrophobic than gold surface (BPT molecule is shown in Chapter 3.2).

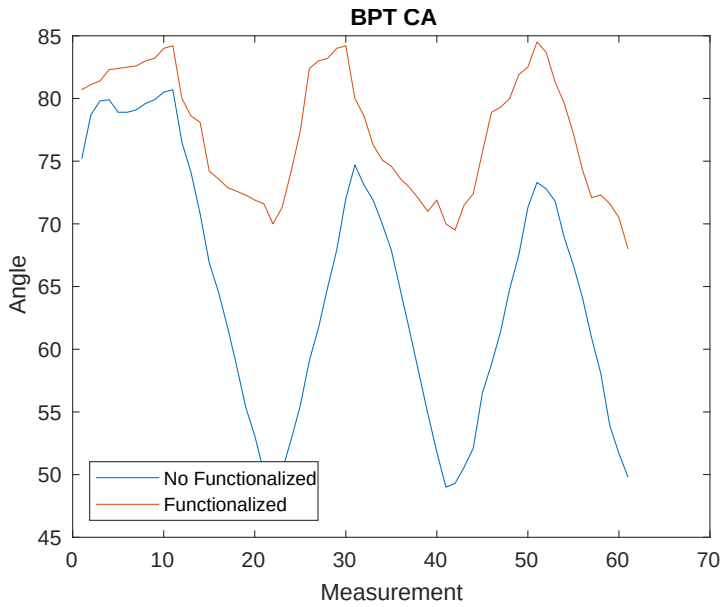

Figure 4.4: Advancing and receding contact angles measurements in BPT functionalized and non-functionalized gold disks sample.

Figure 4.5.a shows a contact angle image from the sample before BPT functionalization, while 4.5.b image was acquired after BPT surface functionalization. In can be noted a significant 10º difference. Functionalization is therefore considered to be coherent. Conversely, in order to ensure the proper placement of BPT molecules, NPs deposition is required, as gold NPs only remain correctly attached if the SAM is coherently assembled.

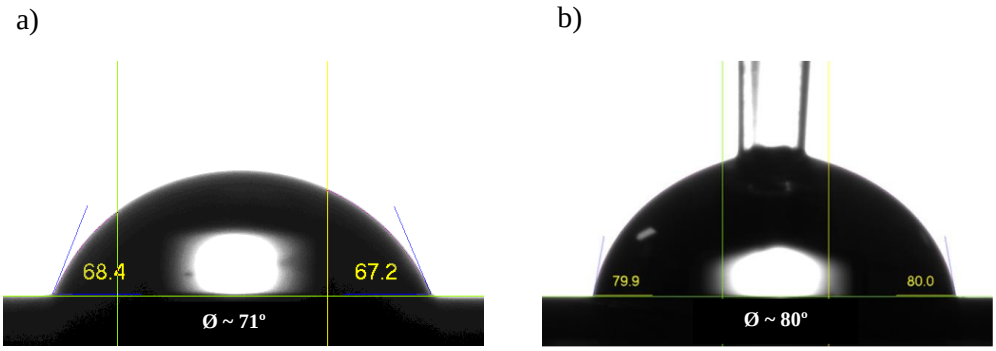

Figure 4.5: a) Non-functionalized gold disks sample contact angle. b) BPT functionalized gold disks sample contact angle.

4.2.1 Micro-contact printing: verification of a new NPs deposition method

As mentioned in Chapter 3, PDMS stamps manufacturing is required to perform this method. PDMS synthesis starts by cleaning the Si master with IPA and drying with N_2. Then, in a disposable galss 0.7 g of curling agent is added to 7 g of base. The resulting liquid elastomer compound needs to be stirred. The latter generates air bubbles, hence sonicating in two five minutes batches is required for remove the bubbles. After removing the bubbles, the master is allocated in a small size vessel, and the elastomer is poured onto the surface, as can be seen in Figure 4.6.a. Then this is introduced on an oven at 90º for 45 minutes to harden the PDMS. Finally, the stamp is squared-shaped using a cutter, resulting the stamp which schematic is represented in Figure 4.6.b.

As can be seen in Figure 4.6.c and 4.6.d, the master dimensions are appropriate for the gold disk lithographed sample. The Si master is constituted by four arrays, resulting of the combination of 2µm squared-shaped meniscus separated 8 µm from each other. Moreover, the disks sample is constituted by four arrays, consisting of 6µm of radius disks, which centers are separated 8µm from each other. However, the same PDMS stamp can be used for NPs transfer to other type of samples. This is caused because the meniscus of the stamps makes the placement of NPs more accurate, thanks to the surface tension generated between the meniscus and the gold patch areas, as can be seen in Figure 4.6.e. PDMS is hydrophobic, while gold surface is hydrophilic, and the NPs solution tends to be adsorbed by the latter once the PDMS stamp is raised. For this main reason, this stamps can be used to place NPs in the SiN wave-guides gold patch samples, provided that the stamp and the sample are correctly aligned, which is something challenging.

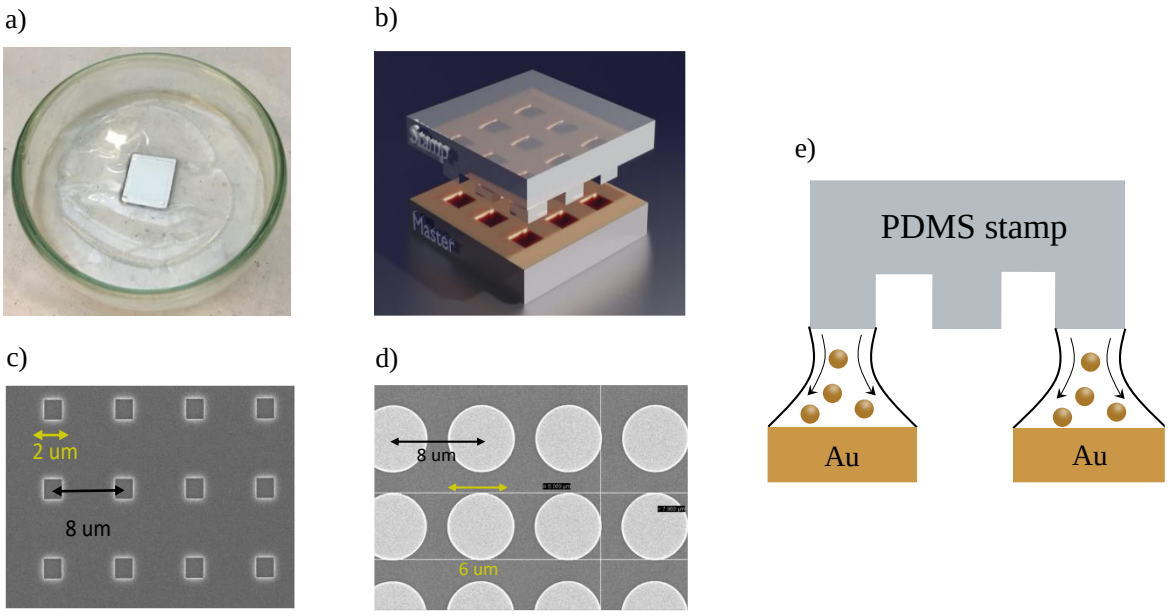

Figure 4.6: a) PDMS poured over the master. b) PDMS stamp and Si master. c) Si Master. d) Gold disks as lithographed sample where the NPs are to be transferred. e) Accurate NPs deposition due to PDMS surface tension.

Figure 4.7 shows an schematic of the micro-contact printing process, performed to obtain accurate stamp-sample alignments. It must be noted that between steps in Figure 4.7.iii and 4.7.iv the sample must be rinsed and dried with N_2. An especial setup, which is shown in Figure 4.8, was used for performing this method. The setup is constituted by a digital camera with zoom and light, a USB camera, a stamp and glass slide holders, an XYZ stage for the sample and a XYZ stage for the stamp. In addition, one computer and a laptop are required in order to control all the possible views. The computer allows to see the XY or stamp-sample surface plane and hence the accuracy of the alignment. Alternatively, the laptop allows to control the transversal plane of both stamp an sample, allowing to measure the distance between them.

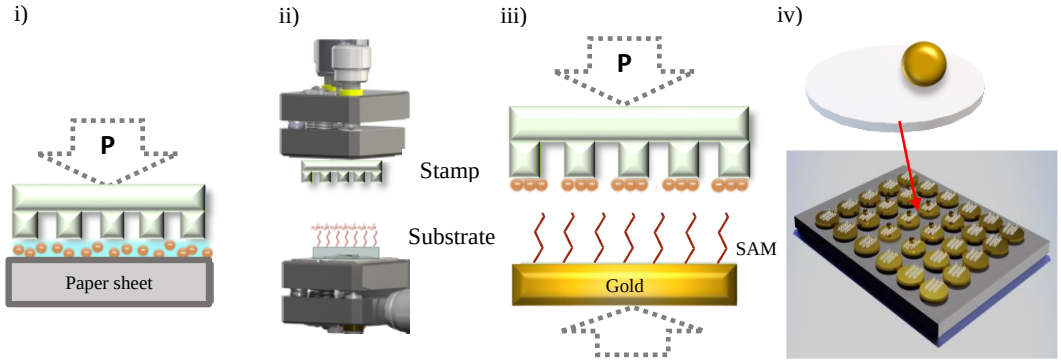

Figure 4.7: NPs transfer process. i) The stamp is pressed against a paper sheet on which 5 µl of NPs solution has been dropped. n. ii) Both stamp and sample are placed at the setup. iii) The stamp is pressed against the sample neatly. iv) Result of transferring NPs to a lithographed sample of gold disks.

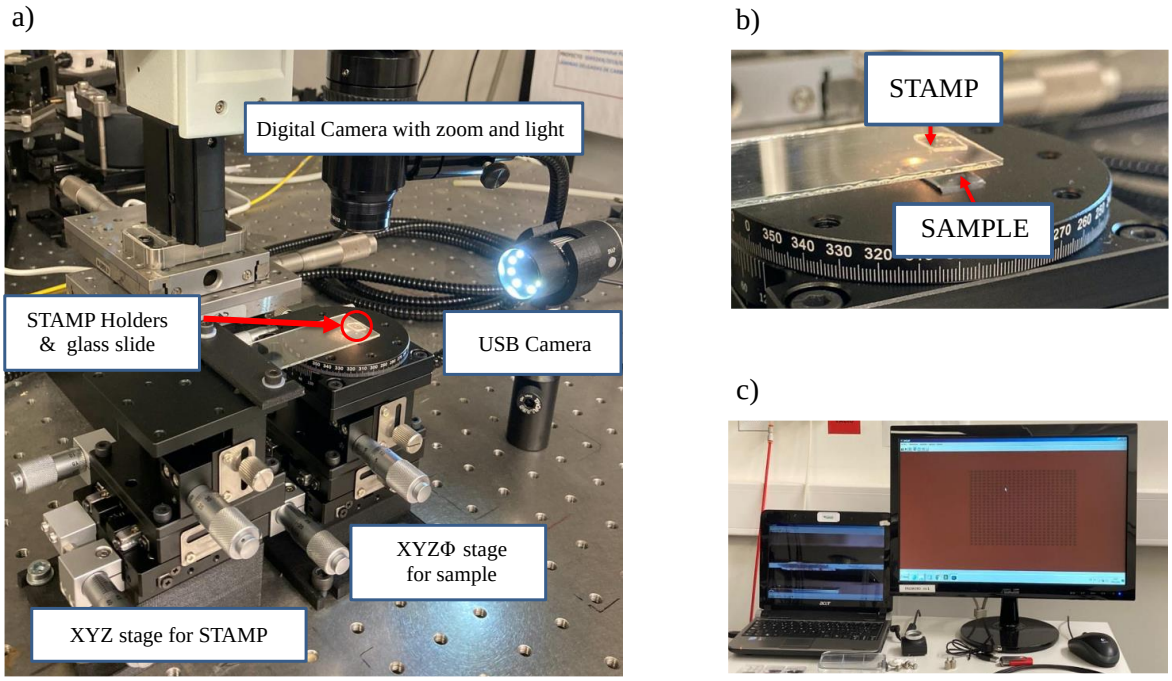

Figure 4.8: Micro-contact printing for NPs transfer setup.

In order to experimentally demonstrate the hydrophobicity of PDMS, before performing NPs deposition it was considered appropriate to measure the contact angle of the PDMS stamp. It is worth to remember that stamps hidrophobicity is the key feature which produces the effectiveness of the method. Figure 4.9 shows the results of the contact angle measurements in PDMS. As can be noticed, its hidrophobicity is remarkable, showing a contact angle of 100º, which is $\approx$ 30º more than gold surface. The basis under the water drop is see-through as PDMS is semi-transparent.

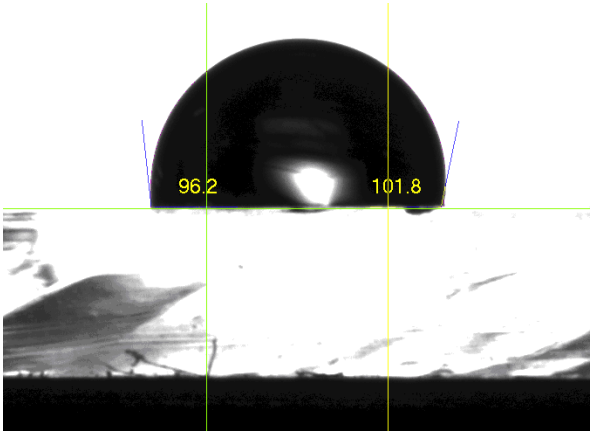

Figure 4.9: PDMS contact angle.

Regarding the stamps manufacturing, Figure 4.10 shows an OM image of the four matrix PDMS stamp obtained from the lithographed master, using the method explained above. It can be noticed that three of the four matrix were properly sealed, while the top-right matrix did not perform particularly successful. This stamp were used to perform the controlled placement of gold NPs.

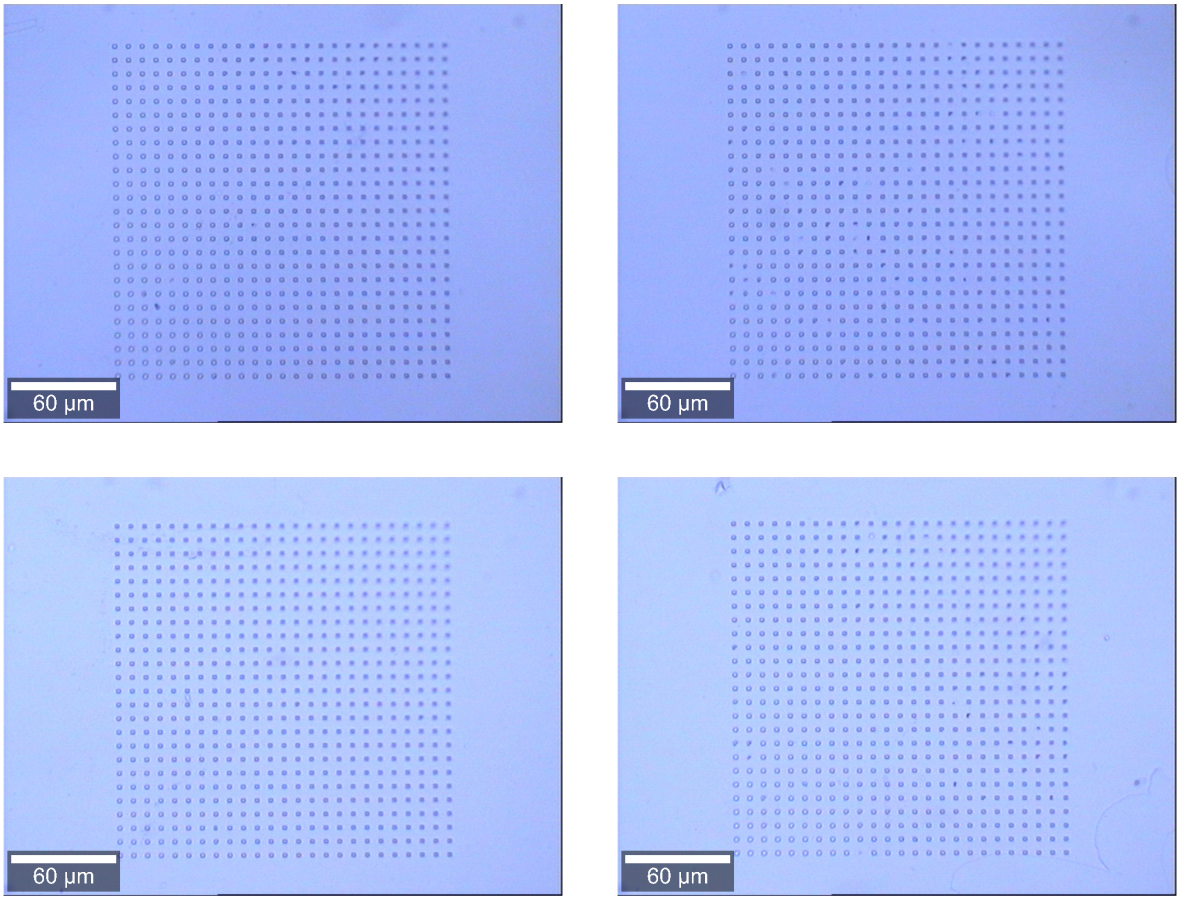

Figure 4.10: Four matrix PDMS stamps acquired from the SiN lithogreaphed master.

After performing 150 nm gold NPs deposition using micro-contact printing technique, the sample was characterized using OM, AFM and SEM. Results showed a very high dependency on the correct positioning during the transfer process. Before showing the results, it should be noted that NPs are brighter in AFM because they are positioned higher than disks; whereas in OM they can be brighter or darker depending on the plane of focus.

AFM characterization

Figure 4.11 shows the AFM images obtained from gold NPs transfer using *micro-contact printing* technique. Figure 4.11.a represents the 3D topography structure from the structure without NPs (left) and with NPs (right). As can be noticed, gold NPs are placed properly onto the gold disks. This 3D images has been acquired from the AFM measures, using the software *WSxM 5.0 Develop 8.1 - Image browser*. In addition, this software has been use to graphically represent the Z-X topography using the 2D images corresponding to the 3D images, as can be seen in Figure 4.11.b. The graphic was obtained by performing a linear tracing on the AFM images. The line can be seen in both images. The red graphic correspond to the line traced on the sample without NPs, while the green one corresponds to the functionalized sample with NPs. It can be noticed a remarkably difference between both graphics,

presenting the green one a peak where the NPs are placed. In addition, the green presents irregular patterns on the disks surface, which may be caused by BPT SAM. It has to be noticed that the height of the disks turned to be 125 nm, which means that some step in the lithography process could have failed, as the disks theoretically measured 233 nm. In addition, the height of the NPs is around 100-150 nm, as expected.

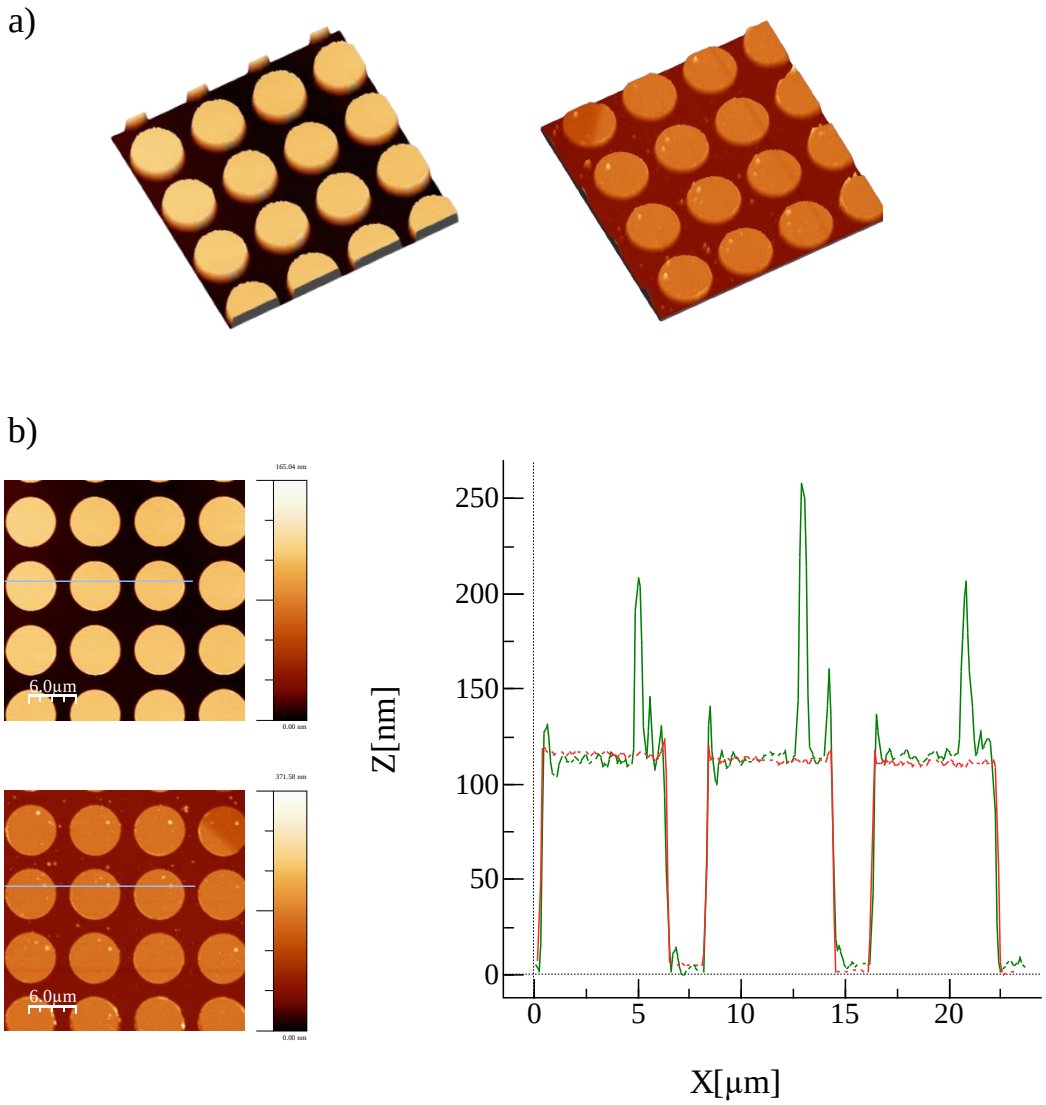

Figure 4.11: AFM images. a) 3D topographic images from both sample without and with NPs. b) topographic measurements represented graphically. The green graphic corresponds to the sample with NPs, while the red references the sample without NPs.

OM characterization

Figure 4.12.a shows OM images, obtained at 50x magnification from the gold disks lithographed sample. The left one corresponds to an area of the sample were the transfer was done accurately, while the right one corresponds to a to a less precise transfer. It has to be noted that the transfer process was performed two times in the same sample. However, in both cases the deposition shows

proper results, as gold NPs are placed onto the gold disks. Alternatively, Figure 4.12.b shows OM images 20x magnification of an area were the NPs are more widely distributed. As can be seen in the left image, a gold NPs cluster has been formed. This could be a result of applying pressure in a non-homogeneous way. The right image, however, shows more coherent results, as several disks show NPs on top of it.

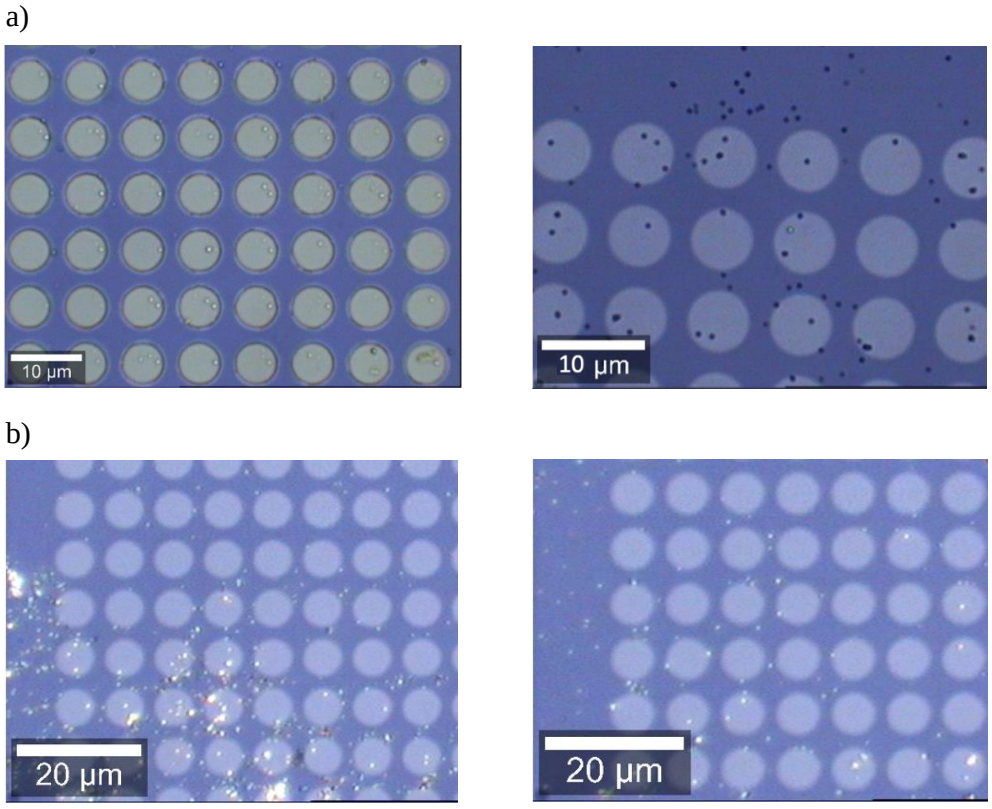

Figure 4.12: a) 50x magnification OM disks-NPs sample images. b) 20x magnification OM disks-NPs sample images.

SEM characterization

Additionally, SEM images have been obtained in order to characterize the plasmonic NP-disk structure. Figure 4.13.a shows two high resolution SEM images obtaines from two NP-disk structure. Figure 4.13.b has been used to prove the NPs dimensions, which results to be 150 nm, as expected. Overall, this method has proven to be effective, as NPs are placed onto or extremely close to the disks, whereas with drop-casting techniques this is a much more challenging task.

Having considered the previous results, it can be stated that the BPT functionalization worked effectively on the gold disks sample. In addition, a new NPs deposition method has been performed and has been proved to work accurately and properly.

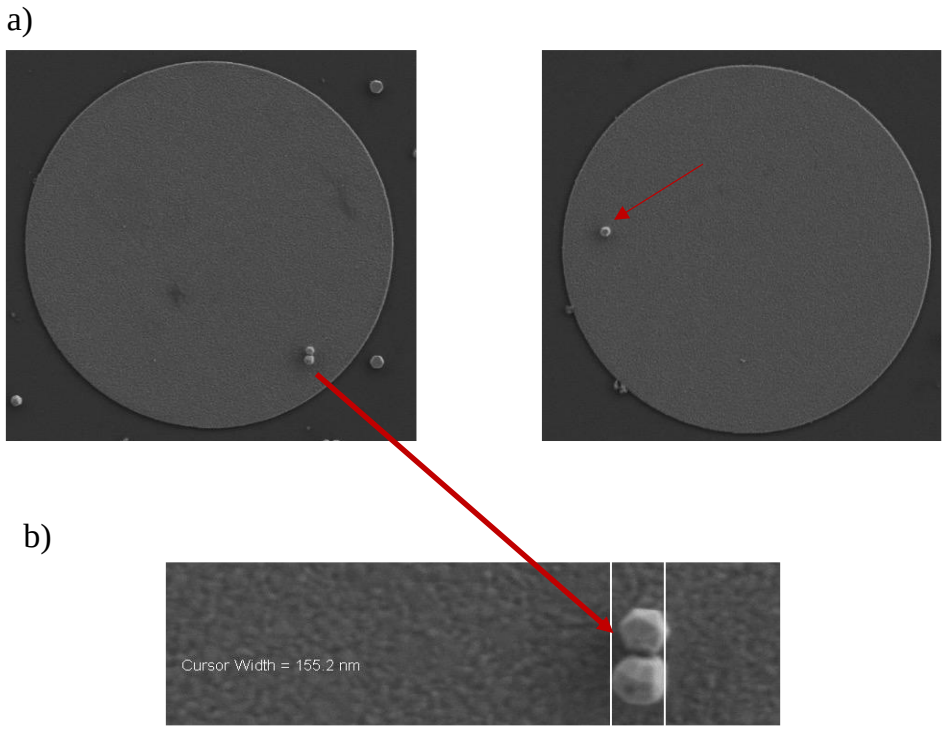

Figure 4.13: a) NP-disks SEM images. b) Two NPs SEM image.

4.3 ABIZ SAM characterization

Due to the already stated relevance of molecular optomechanics, it was decided to continue this project by studying new molecules that perform more efficiently than BPT in the THz range. This new molecule is ABIZ, and it is labeled as *new* because only few studies has been done with it. The results showed in this section are to be published. Additionally, after characterising the disks, this project continued on another line of photonic structures that allow guided light collection and transmission, due to the importance of integrating photonic circuits on chips.

4.3.1 ABIZ: a new method to perform SAMs

Scarce studies using ABIZ to functionalize surfaces at room temperature have been found. In [55] a SAM using ABIZ is performed in order to functionalize an Au electrode. However, the recipe provided was not consistent for the present work, as the application of the study was not similar and extremely high concentrations were used. Therefore, it was decided to develop a new recipe, using significantly lower concentrations, in the order of a 10^3 times lower. In addition, the foundation of this recipe was based on scientific evidence on SAMs performed with thiols [56]. The new ABIZ functionalization recipe is detailed below:

- Dump 20 ml ethanol in a beaker.
- Place cling film on the scale and pour in ABIZ (solid) to 33 mg, which corresponds to a 10 mM concentration.

- Pour the ABIZ over the 20 ml ethanol and mix softly. Figure 4.14.a shows the result of this step.
- Immerse the sample into the solution, ensuring to place the lithographic surface facing upwards. Figure 4.14.b shows the result of this step, using three samples (non-lithographed).
- Leave two sample immersed for 16 hours hours and one sample for 43 hours. (Note that the different time periods were performed in order to compare the results and see which gave the most consistent SAMs).
- Extract samples, immerse in ethanol and sonicate for three minutes.
- Dry with N_2.

a) b)

Figure 4.14: a) 10 mM ethanol-ABIZ solution. b) Three Si samples with gold evaporated on the surface for ABIZ functionalization time validation.

After performing the previous method, a combination of methods and characterisation techniques were applied to confirm the viability of the SAM. The results are explained throughout this section.

4.3.2 ABIZ functionalization verification

For the ABIZ functionalization verification, five non-lithographed samples were used. This samples were SiO2 samples with a gold layer at the surface. Figure 4.15 shows an schematic of the verification process. One of the samples (S0) was used to measure the contact angle, remaining non-functionalized throughout the study. The other four samples were functionalized. Two of them (S1 & S2) remained 16h in the chemical ABIZ solution for perform functionalization, while the fourth (S3) one remained 43h. One of the 16h sample (S1) was used to measure the contact angle after functionalization in two points of the sample. S2 was used for ABIZ SAM characterization after having checked the differences in CA between S0 and S1. S3 was also characterized. The last sample (S4) was functionalized for 16h for corroborate the stability of the 16h method.

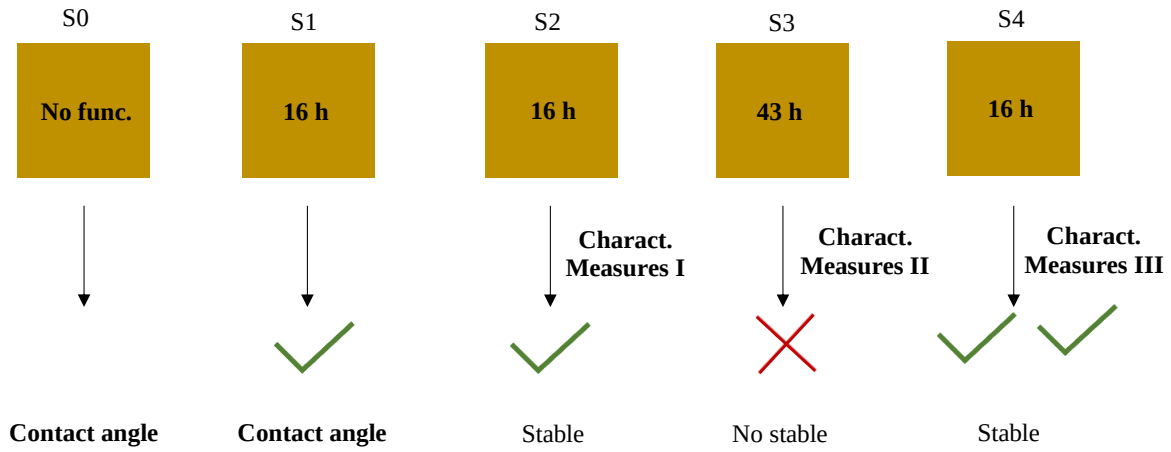

Figure 4.15: Schematic of the ABIZ SAM verification process.

Contact Angle measurements

S0 and S1 were used to measure the differences between an ABIZ funcionalized surface and a non-functionalized gold surface. Figure 4.16 shows the results of the CA measurements, which corresponds to the advancing and receding contact angles of one point in S0 (blue graphic) and two points in the S1 (orange and yellow graphics). It can be noticed a remarkably difference of $\approx 10^{o}$ between functionalized and non-functionalized CA measures, stating that SAM exists in S1.

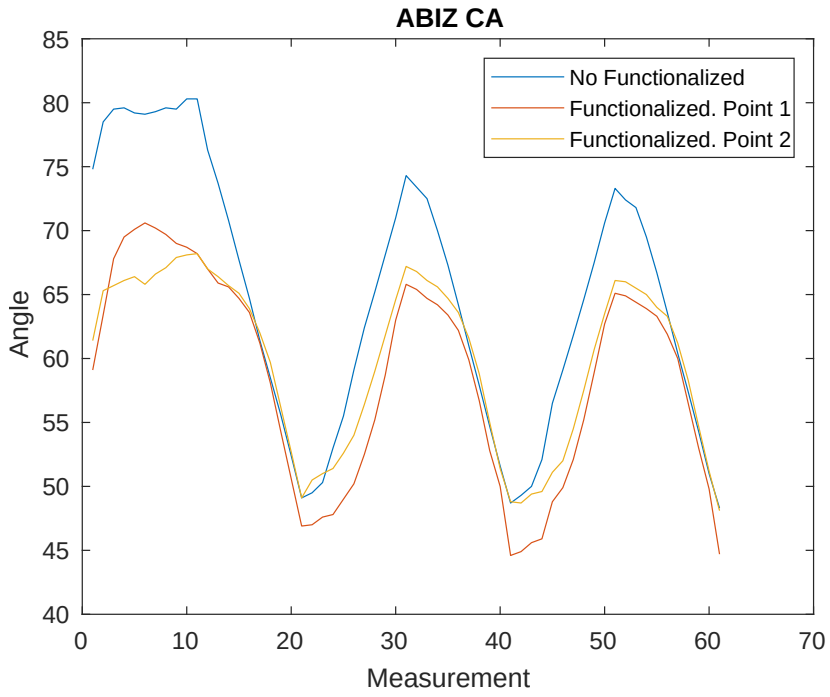

Figure 4.16: Advancing and receding contact angle measurements. The blue graphic corresponds to S0 sample, while the orange and the yellow correspond to two different points of S1 sample.

Additionally, Figure 4.17.a shows a CA of S0, which value is around 70º, while S1 presents a CA of approximately 60º. As can be noticed, ABIZ SAM provides more hydrophilic surfaces when comparing with gold surface. This result was expected, as ABIZ molecules presents an amine group and other N groups, which can create dipoles with water, making the surface more hidrophilic.

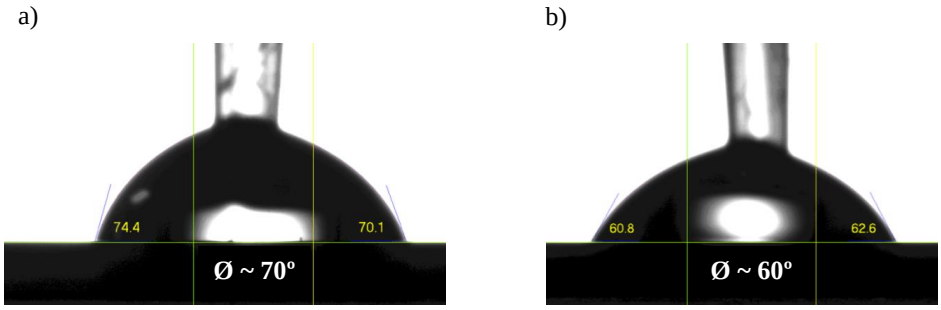

Figure 4.17: a) Non-functionalized gold surface CA. b) ABIZ functionalized surface CA.

Gold NPs characterization by DLS

Before characterizing the SAMs and nanophotonic circuits having performed NPs deposition, it was considered necessary to characterize the gold NPs used in this project, as plasmonic structures response depends directly on the size, shape and composition of the NPs. For this reason, DLS of labeled spherical gold 60 nm NPs were performed. Results shown that these were negatively charged and the Z potential of the solution is -52 mV. This is a relevant feature, as protonation technique provides better results if negatively charged NPs are used after. In addition, Figure 4.18 shows the average size measured, which was $\approx$ 65 nm. One can notice that even labeled verified products may not strictly meet the specifications. This can lead to unexpected results being incorrectly associated with characterisation or even design errors. Therefore, performing this analysis has been considered a good practice.

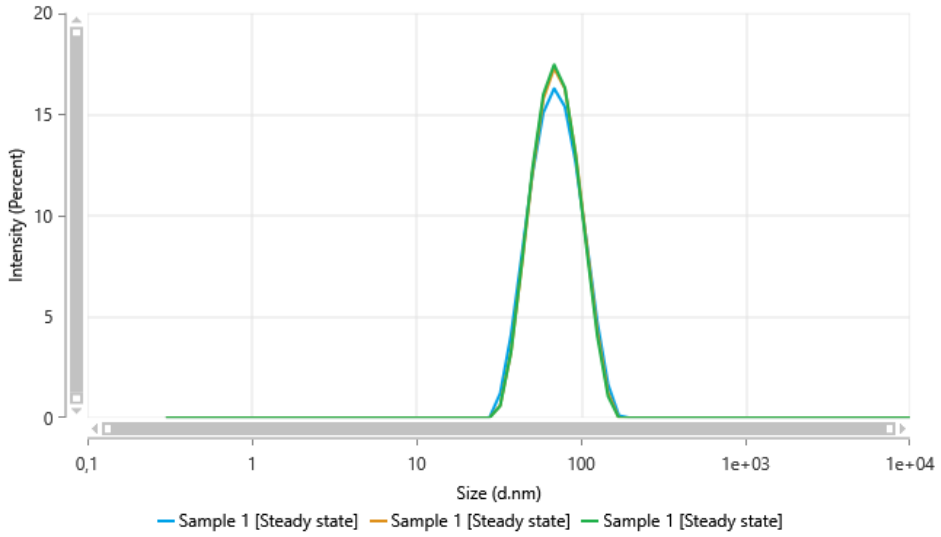

Figure 4.18: NPs average size at characterization by DLS.

NPs deposition by drop-casting technique

Figure 4.19 shows the result of NPs drop-casting, performed onto one of the non-lithographed samples (S2). 8 µl of the NPs solution were dropped en each sample, then remained five minutes, rinsed with water and dried with N_2.

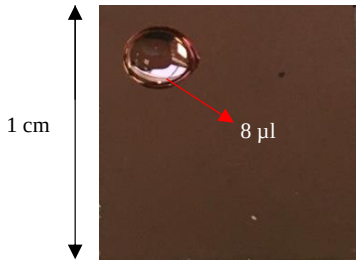

Figure 4.19: NP deposition by drop casting.

AFM characterization

An AFM measurement was performed to check the surface uniformity and discard possible clusters of molecules. Figure 4.20.a shows a topographical representation of S2 sample, measuring 15x15 µm. As can be seen, S2 surface presents homogeneity, excluding the possibility of molecular aggregates forming. Additionally, 4.20.b shows S2 sample after performing drop-casting technique. NPs are bonded to the Au surface. This indicates the success of the functionalisation, although further measures were needed for verify the SAMs stability, as will be discussed below.

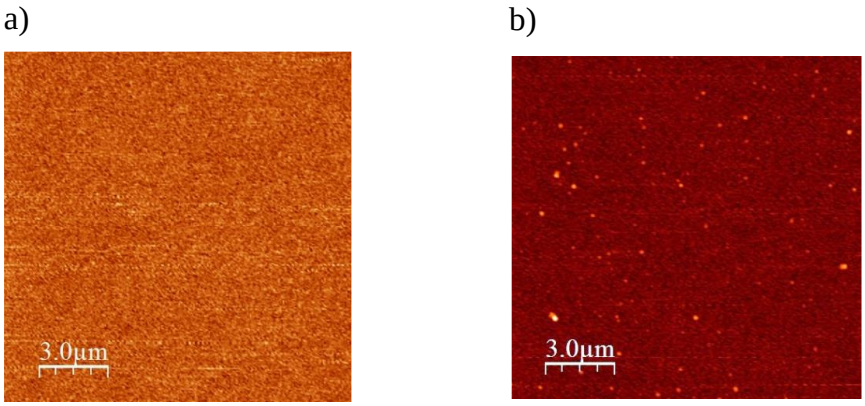

Figure 4.20: AFM images. a) S2 AFM topographic image. b) S2 AFM topographic image after performing NPs deposition. As NPs are higher that the surface, these are represented with higher intensities.

Protonation using HCl

ABIZ is linked to the gold surface thanks to the thiol group, while the amine group is responsible of bonding the molecule to the gold NP. As has been noted, gold NPs are negatively charged, so they are

attracted to positive charges. It is possible to enhance the affinity between ABIZ and NPs, using the protonation method. As mentioned in Chapter 3, for ABIZ protonation a solution composed by HCl and MiliQ water was used, being the relation 1:100. Here 20 ml of MiliQ water and 20 µl of HCl has been used. The samples to be protonated must remain five minutes in the MiliQ-HCl solution, then rinsed with water and dried with N_2. Figure 4.21 shows an schematic of protonation. The surface will be positively charged and more NPs will adhere to the surface. It should be noted that protonation is also a way to check the SAMs stability, as if this method only works where SAMs are coherent. Results before and after protonation are shown below.

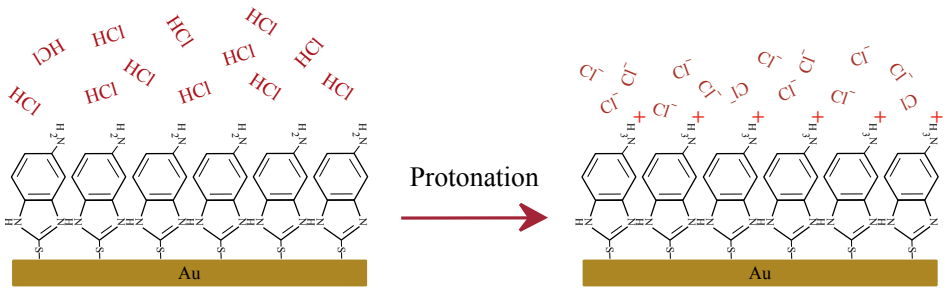

Figure 4.21: Protonation method using HCl as strong acid. .

OM and DFOM characterization

As mentioned in 3, the OM is integrated in the Raman equipment, and it is usually used for positioning the sample at the interest area. In order to compare the results, OM and DFOM images of S2, S3 and S4 were obtained.

First, it was considered necessary to compare the differences between non-protonated and protonated samples, as this method has been applied to every sample **after confirming SAMs stability with SERS**. Figure 4.22 shows S2 and S4 OM and DFOM images. Figure 4.22.a and 4.22.b are S2 OM images, before and after protonation, respectively. Comparing both images, a remarkably increase on the NPs density can be noticed. Regarding S4 sample, Figure 4.22.c corresponds to an OM image before protonation, while Figure 4.22.d corresponds to an DFOM image. A contrast can be identified by comparing the two latter images. Overall, protonation method has been proved to be effective. Additionally, the efficiency of the method is also an evidence of a proper SAM performance, as molecules should be properly assembled for this method to work.

Regarding S3, Figure 4.23 shows OM and DFOM images from diverse areas from the sample **without protonation**. Figure 4.23.a shows an OM image a few NPs, while Figures 4.23.b, 4.23.c and 4.23.d are OM and DFOM images of samples defects, where NPs got stuck. Apparently, one could think that functionalization could have worked properly, but this statement must not be assumed until Raman spectroscopy confirms the correct assembly. As mentioned, this sample was not protonated, as its Raman spectrum showed results of instability, which will be explained below.

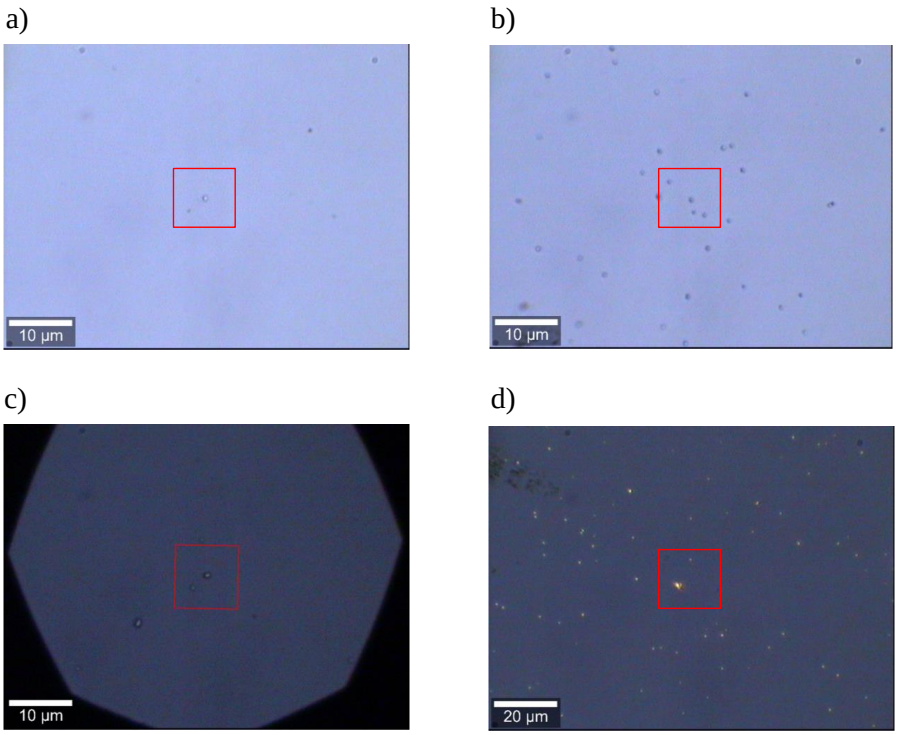

Figure 4.22: 50x magnification images. a) OM image, S2 sample before protonation. b) OM image, S2 sample after protonation. c) OM image, S4 sample before protonation. d) DFOM image, S4 sample after protonation.

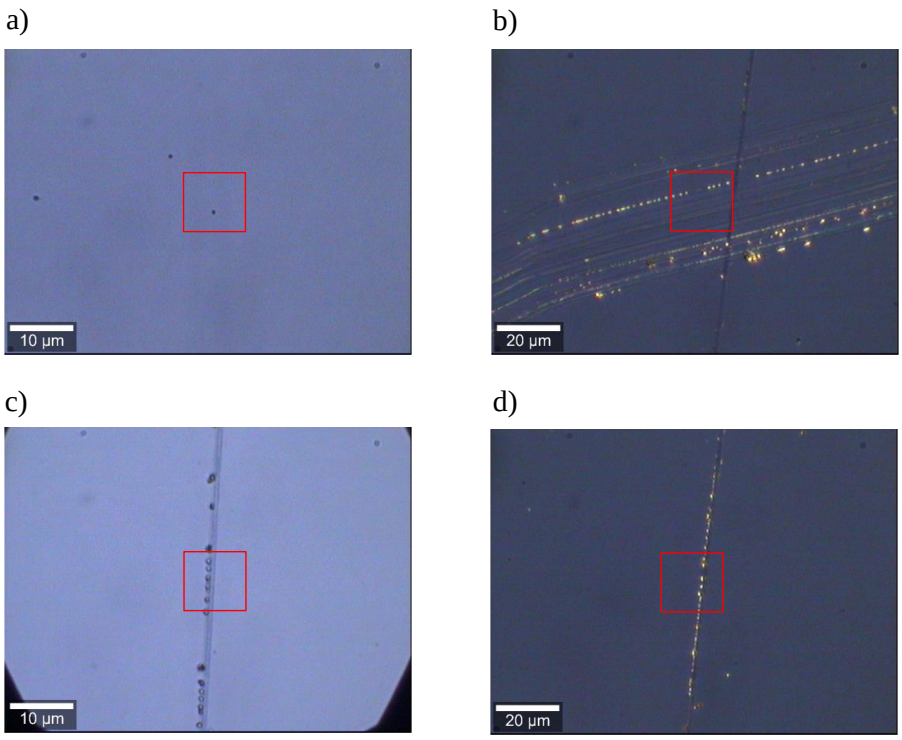

Figure 4.23: S3 50x magnification images. a) OM high NPs density region. b) DFOM, NPs deposited on sample defects. c) OM, NPs deposited on a grate d) DFOM, NPs deposited on a grate.

Raman−SERS measurements

In this work, Raman measurements were performed in order to detect the presence of ABIZ and for determining the stability of S2, S3 and S4 samples. As explained in Chapter 2, one effective way to acquire single molecule Raman spectrum is performing SERS. Here, NPoM structure is used to enhance the ABIZ molecule Raman spectrum, as NPs are separated from the gold surface through ABIZ molecule and it inelastic scattering signal is enhanced. The SERS spectra obtained must have similar characteristics to determine the stability of the SAM. The spectrum provided by [47] was used to verify the spectrum obtained experimentally. In addition, only the best normal vibrational modes (above 700 cm^{-1} and below 1700 cm^{-1}) have been consider to characterize the ABIZ spectra and determine the stability. Figure 4.24 shows the reference spectrum.

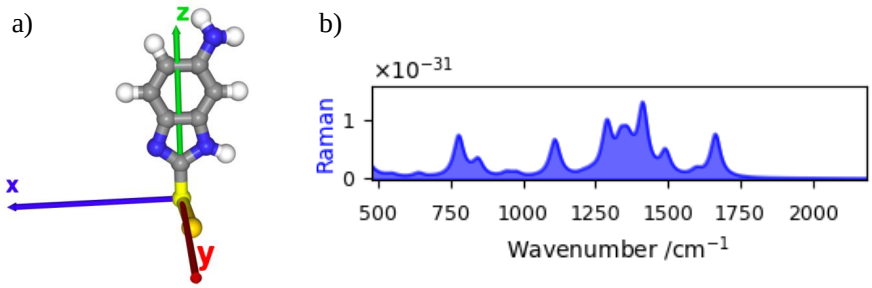

Figure 4.24: a) ABIZ molecule orientation. b) Raman spectrum obtained by simulations, considering a 532 nm laser, x-beam polarization and ambient conditions.

In this study, two types of Raman measurements have been performed, which depend on the laser employed. Both green monochromatic laser (532 nm wavelength) and red monochromatic laser (633 nm wavelength) belong to the visible EM region. Consequently, LSPR is excited in both scenarios. However, differences in the spectra have arisen due to fluorescence effect caused by the interaction between the green laser with the gold, generating a wide spectrum from 2000 cm^{-1} onwards. In addition, wavenumber values were remarkably affected by a background effect. This was associated with the presence of noise, probably caused by the photothermal effect generated by the laser (independently the laser wavelength).

First, Raman measurements were performed to compare S2 and S3 samples, as functionalization times were different. Figure 4.24.b and [57] were used to compare and validate ABIZ spectrum. These Raman spectrum were obtained using the red laser (633 nm), P = 26 mW, G = 600. Figure 4.25 shows the Raman spectrum obtained on two NPs of S2. Figure 4.25.a is the 1600 cm^{-1} shift sample response, which is known corresponds to the amine stretching vibrations [57]. Figure 4.25.b corresponds to the 1250 cm^{-1} shift sample response. Spectrum a) was obtained from the left NP, while Spectrum b) was obtained from the right one. Both were compared with 4.24.b and with the molecular vibrations specific to mercaptobenzimidazole group. Results show the existence of a correct self-assembled ABIZ monolayer, as Raman peaks are coherent.

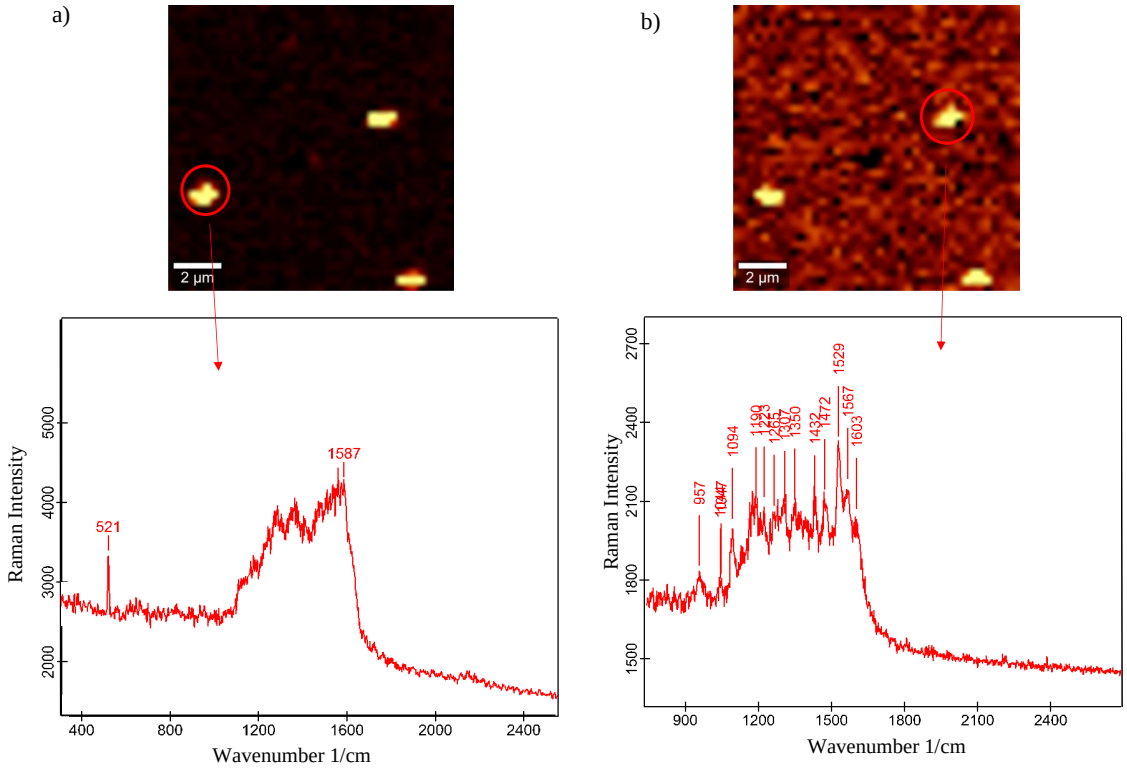

Figure 4.25: Raman images obtained at for 1600 cm^{-1} shift (left) and for 1250 cm^{-1} shift (right) a) S1, left NP Raman spectrum. It has to be noticed that the 521 peak is corresponds to the Si peak. b) S1, right NP Raman spectrum.

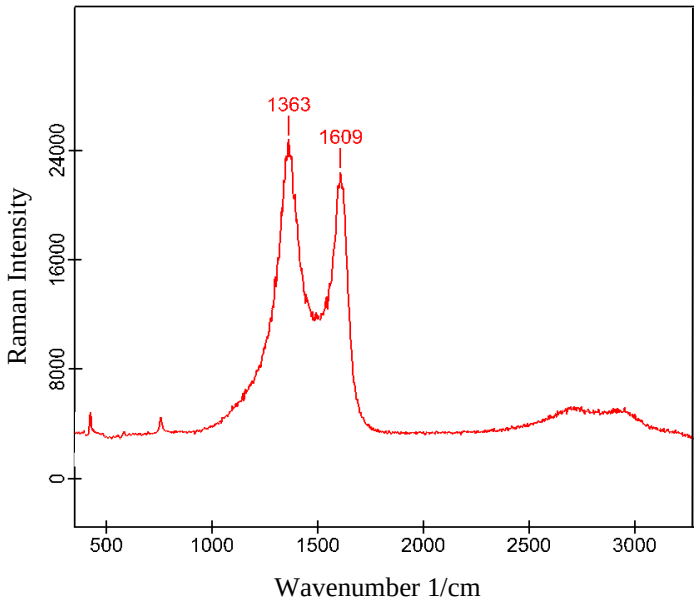

Figure 4.26: S3 NP Raman spectrum.

Alternatiely, Figure 4.26 shows the Raman spectrum obtained for one of the S3 NPs showed in Figure 4.23. As can be seen, the spectrum is different from the ones obtained in S2, and it also presents remarkably differences when comparing with the reference spectrum in Figure 4.24.b. Therefore, it was classified as an unstable functionalization, discarding the 43h functionalisation sample and recipe. It has to be noted that the SERS phenomenon occurred in both samples, independently of the SAMs stability, as it results from the NPoM configuration.

Secondly, the S4 NPs Raman spectrum were obtained using the green laser (532 nm), P = 7 mW, G = 600. It was considered using the green laser to characterize this sample, as the SPR is activated more effectively at more energetic optical frequencies [24]. However, the fluorescence effect appeared from 2000 cm^{-1} shift above. Figure 4.27.a shows a few S4 NPs image obtained from a Raman 1600 cm^{-1} shift. Figure 4.27.b shows one of the S4 NPs image obtained from a Raman 1600 cm^{-1} shift. Both Raman spectra represented in Figure 4.27.c and 4.27.d graphics were obtained from Figure 4.27.b. While Figure 4.27.c shows the Raman spectrum obtained in the most external areas of the NP but not in its center, Figure 4.27.c shows the Raman spectrum obtained in the NP center. It can be noticed that the fluorescence effect is highly intensified in the NP center, while the ABIZ spectrum can be seen in both of them despite the background effect generated by the fluorescence. The presence of a stable ABIZ SAM in S4 is therefore confirmed.

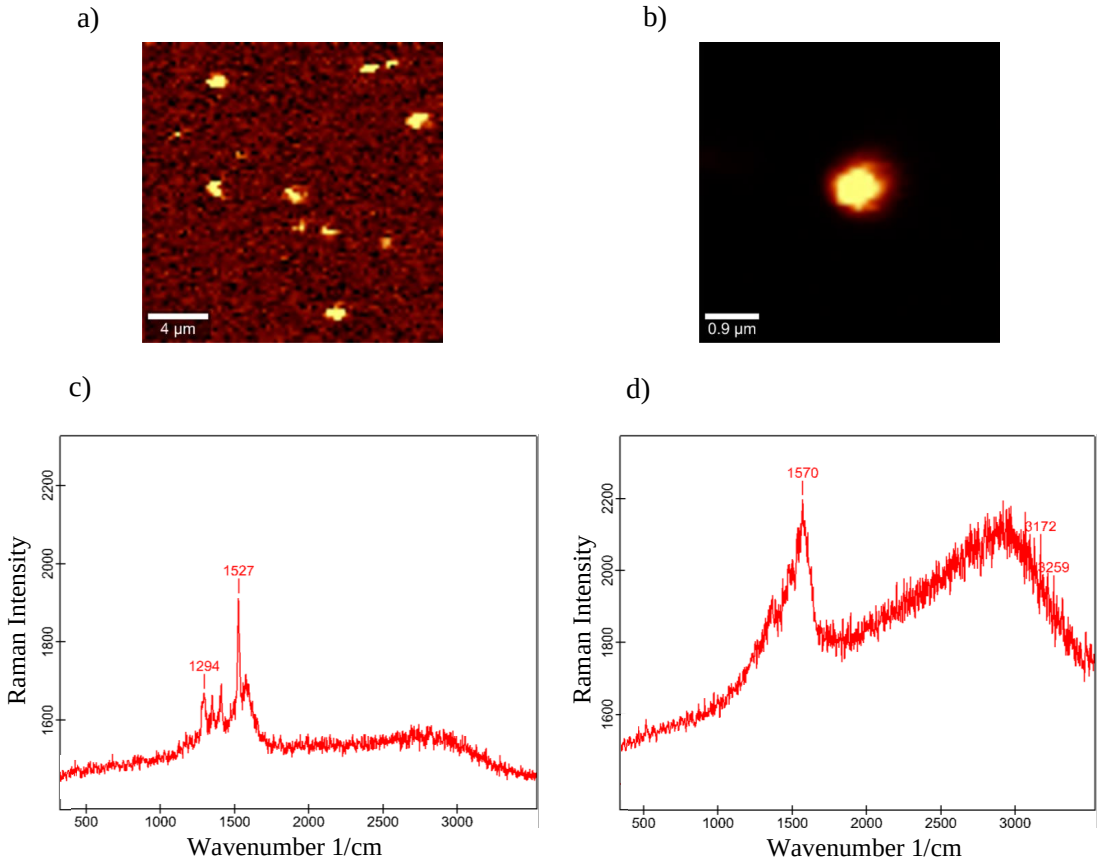

Figure 4.27: S4 Raman results. a) 4x4 µm 1600 cm^{-1} shift Raman image. b) 0.9x0.9 µm 1600 cm^{-1} shift Raman image. c) Raman spectrum above b) NP. d) Raman spectrum at the center of b) NP.

It should be noted that due to laboratory limitations the exact molecule orientation cannot be known. In addition, the photothermal effect generated by the laser itself generates the signal background amplification. These two limitations have to be taken into account when comparing the spectra. Nevertheless, the strongest ABIZ peaks can be resolved experimentally, so it can be concluded that exist a stable and coherent self-assembled monolayer and that this is verified by the NPoM-induced SERS effect.

4.3.3 Orthogonal wave-guides with intersection gold patch

In order to verify that ABIZ SAM can be performed on lithographed circuits, two types of samples have been used. In this section the functionalization of orthogonal wave-guides structure, consisting of six 5000x600 nm SiN orthogonal guides with a 600x600 nm gold patch on the intersection, will be studied. Figure 4.28.a and 4.28.b shows an schematic of this structure. The guides were orderer from one to six from left to right. Figure 4.28.c and 4.28.d correspond to OM images of wave-guide number 3, before the sample functionalization. After functionalization, 150 nm gold NPs transfer was performed using *micro-contact printing* technique. OM, SEM and Raman characterization results are shown below.

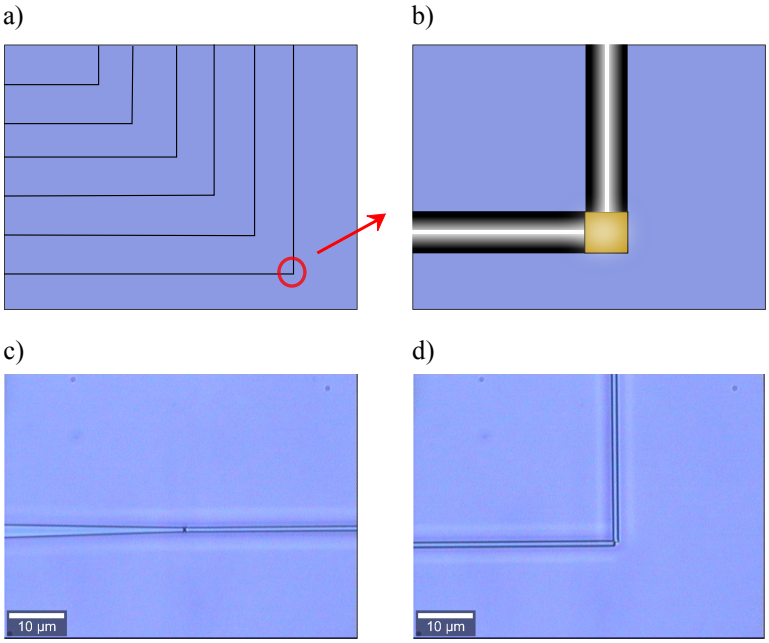

Figure 4.28: SiN Orthogonal guides lithographic structure. a) Schematic representation of the six orthogonal SiN wave-guides. b) Intersection of two guides, where the gold patch can be seen. c) 50x magnification OM image, guide 3. d) 50x magnification OM image, guide 3 intersection.

SEM characterization

Figure 4.29 shows the images resulting with SEM technique of two different samples with the same lithographed structure. As can be seen, the gold patch is positioned slightly above one of the orthog-

onal guides, and this occurs in every intersection of both samples. This is due to a lithography error. However, this did not prevent the NPs from being successfully deposited on the gold path. Figure 4.29.a and Figure 4.29.b are guides from one sample, while 4.29.c and Figure 4.29.d are guides from another different sample equally lithographed. Figure 4.29.a, 4.29.b and 4.29.d shows NPs deposited at the gold patch surface, while Figure 4.29.c does not present NPs. Even though Figure 4.29.d (sample 2, guide 3) does not present the NP deposited in the middle of the patch, it is considered a success that it has stuck to the end, as it shows that the ABIZ functionalization has been effective.

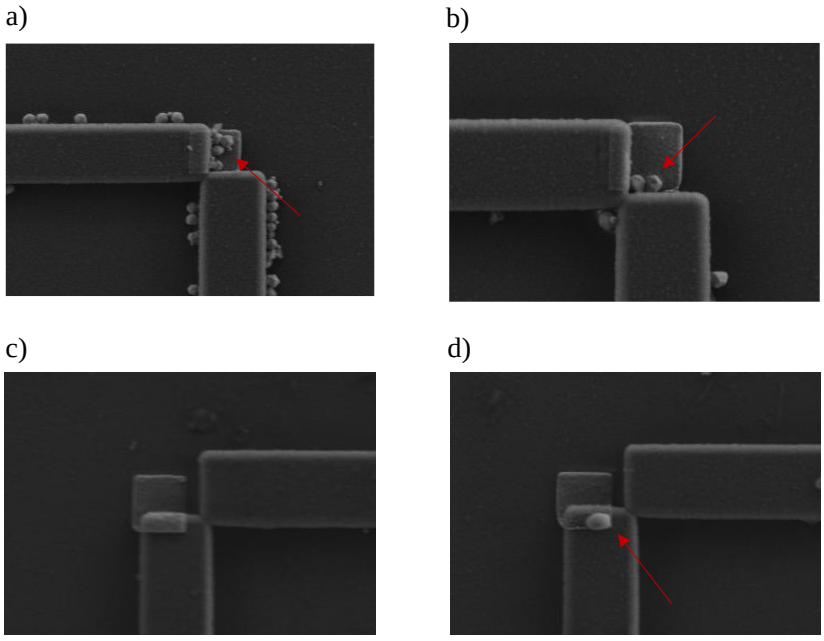

Figure 4.29: Orthogonal SiN wave-guides SEM images. a) Lithographed sample 1, guide 2. b) Lithographed sample 1, guide 4. c) Lithographed sample 2, guide 1. d) Lithographed sample 2, guide 3.

Raman characterization

For this samples, Raman spectrum were obtained using the green laser (532 nm), P = 7 mW, G = 600. Figure 4.30.a represents the Raman signal image obtained for a 521 cm^{-1} shift, which represents the SiN structure response of the guide number 3, sample 2, represented in 4.29.d. Alternatively, Figure 4.30.b represents the Raman signal image obtained for a 2000 cm^{-1} shift of the guide number 3, sample 2. As can be seen, only the gold structure can be seen, and SiN cannot be observed, as fluorescence is an intrinsic effect of gold in this structure. Regarding the orthogonal guide 3, observed in Figure 4.29.d, two Raman spectra were obtained. Figure 4.30.c represents the Raman spectra obtained at the center of the gold patch, where no NPs can be found. The graphic shows the fluorescence effect, logically without presence of the ABIZ spectrum, as there is no NPoM structure. Alternatively, Figure 4.30.d represents the Raman spectra obtained on top of the NP. Despite presenting fluorescence background, it can be noticed the ABIZ Raman spectrum. Therefore, it can be concluded that the functionalization was coherent and that NPoM configurations are also possible in this type of structure.

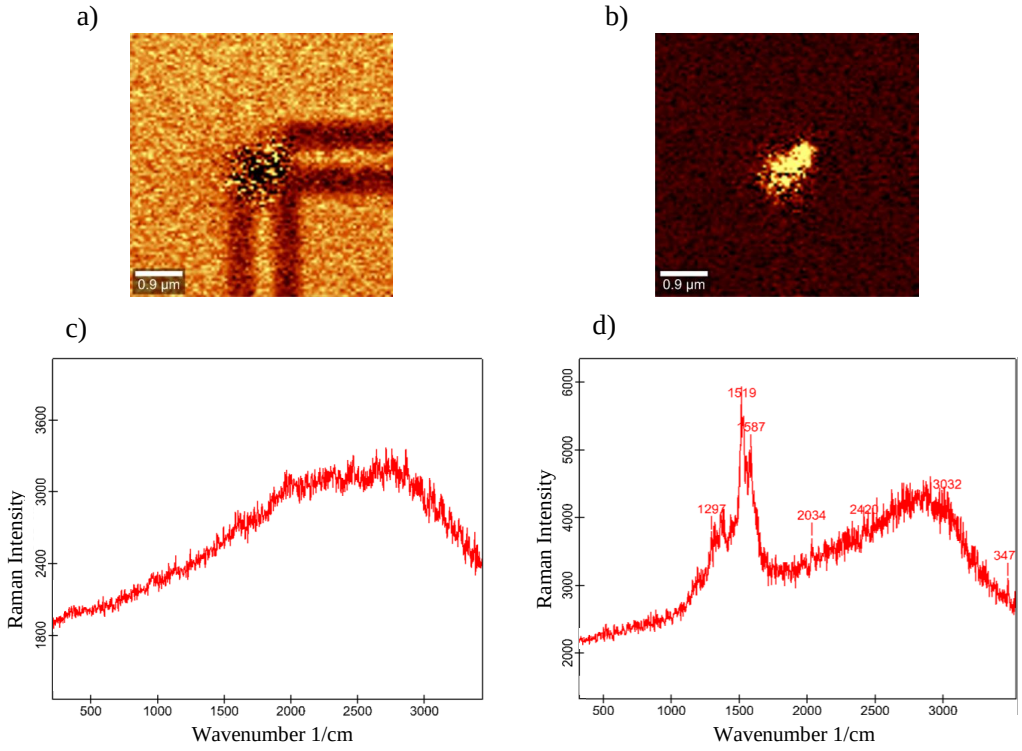

Figure 4.30: a) Raman image, 521 cm^{-1} shift (guide number 3, sample 2). Raman image, 2000 cm^{-1} shift (guide number 3, sample 2). c) Raman spectrum (guide 3, sample 2, at the center of the gold patch). d) Raman spectrum (guide 3, sample 2, at the center of the gold NP).

4.3.4 SiN wave-guides with surface gold patch sample

Lithographed Si samples consisting of six 5000x600 nm SiN guides with a 1000x500 nm gold patch on top of each were functionalized with ABIZ. Figure 4.31 shows DFOM (4.31.a) and AFM (4.31.b) images from number 5 SiN guide before its functionalization. In both images, the gold patch can be seen across the SiN guide. The patch is slightly wider than the guide, serving as an anchor in the Si base. *Micro-contact printing* was used for 150 nm NPs deposition.

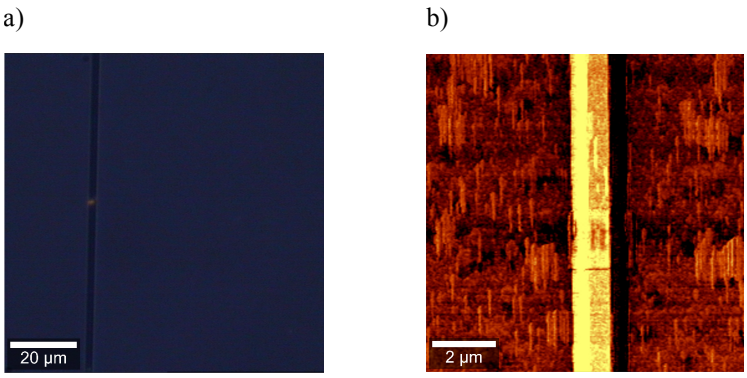

Figure 4.31: Patch 5 images. a) DFOM 50x magnification image. b) 2x2 µm AFM image.

DFOM characterization

Figure 4.32 shows the DFOM images obtained from two of the six guides. While 4.32.a shows guide 3 and 4, 4.32.b shows only guide 4. The rest of the guides gave hardly any signal in DFOM, as there were no NPs around the patch. Both images show how the NPs were placed at the junction of the patch and the Si, and not on top of it, as intended. SEM images confirmed lately this event.

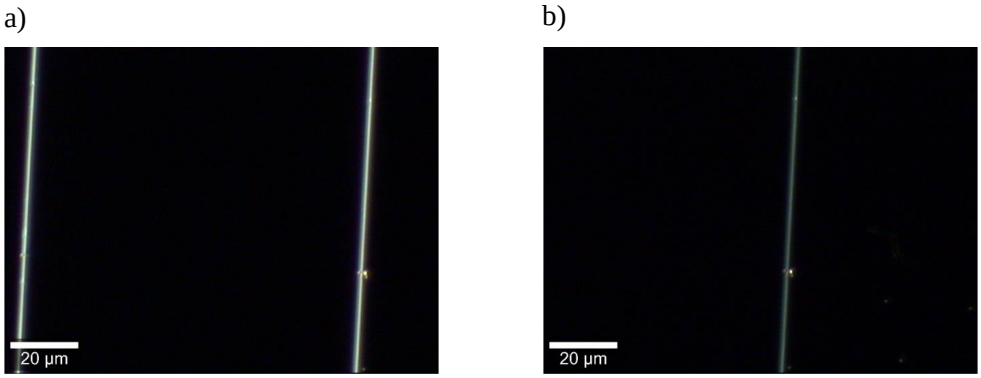

Figure 4.32: DFOM SiN guides with gold patch 50x M images. a) Guides 3 and 4. b) Guide 4.

SEM characterization

Figure 4.33.a shows guide 1 SEM image, and it can be seen that the NPs deposition went wrong, probably as a result of an non-homogeneous pressure while performing *micro-contact printing* method. Figure 4.33.b shows guide 2, and a smaller NP deposited in the Si-patch joint. Figures 4.33.c and 4.33.d are guides 3 and 4, shown in Figure 4.32.a, which show NPs deposited on the gold joint.

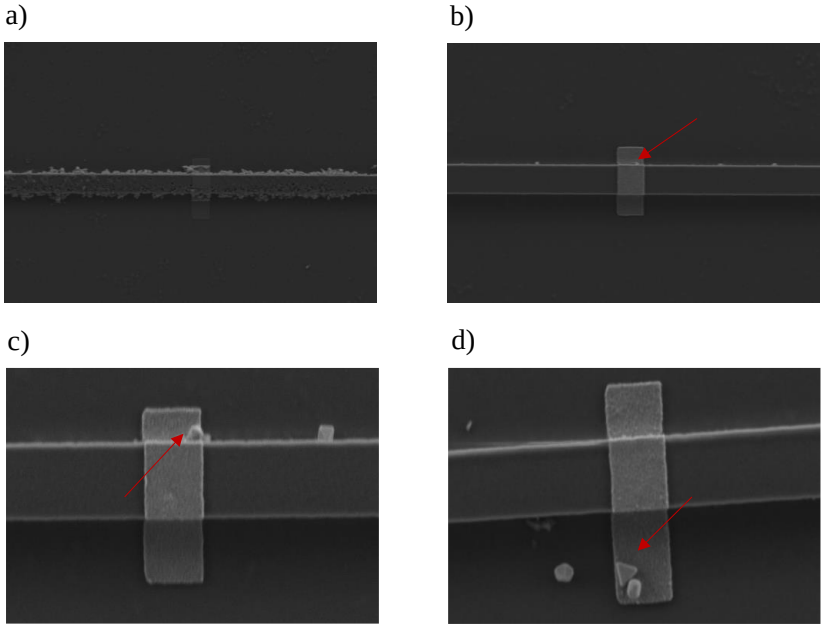

Figure 4.33: SEM SiN guides with gold patch images. a) Guide 1. b) Guide 2. c) Guide 3. d) Guide 4.

Raman characterization

In order to verify the ABIZ functionalization, Raman spectrum were obtained from guide 4. Figure 4.34.a shows the Raman spectrum obtained on top of the gold patch, using the green laser (532 nm) P = 7 mW, G = 600, where no NP was found. It can be seen the fluorescence effect, but without ABIZ spectrum evidence. Alternatively, Figure 4.34.b shows the Raman spectra obtained using the red laser (633 nm), P = 26 mW, G = 600, from the NP top. ABIZ spectrum can be identified, resulting from the NPoM configuration.

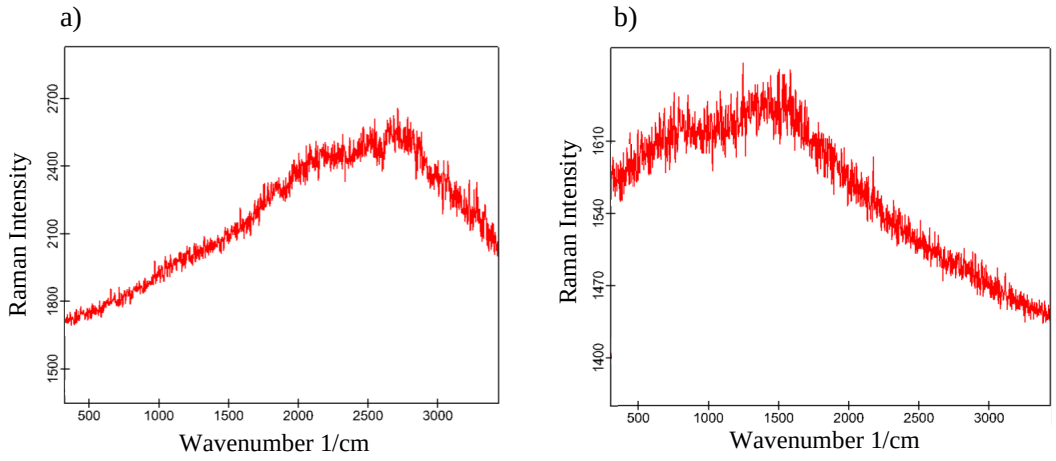

Figure 4.34: SiN guides with gold patch Raman spectra, guide 4. a) Raman spectrum obtained on top of the gold patch, no NP. b) Raman spectrum obtained on top of the gold NP.

Although the NPs deposition technique was not particulary useful in this case, the stability and effectiveness of the ABIZ functionalization can be confirmed.

4.4 WERS: development of a new setup

The WERS setup was assembled in combination with a Near-field Scanning Optical Microscopy (SNOM) setup, since this latter provides relevant features. SNOM in WERS can be used as an alternative mode of excitation of the near-field structures, where alternative modes of vibration could be excited. In addition, SNOM measurements can be done, which is an additional useful tool that could ensure the guide is performing in a proper conditions. This is mainly because when the signal passes properly through the guided structure, the SNOM signal is different than when it does not, as the excitation of the NPoM structure above the guide depends on it. For the assembly of WERS-SNOM setup, it was necessary an optic microscope for sample positioning, the laser inputs via fibre optics, the SNOM probe (Cr and Au alloy tip), SNOM probe positioning equipment, two XYZ positioning stages, sample positioning stage, a USB camera, an objective, optic fiber, one computer, a laptop, and 3D printed pieces.

Figure 4.35.a shows the resulting WERS-SNOM setup. The input signal (1400-1575 laser) is guided by a optic fibre until it reaches the sample. Alternatively, the signal is collected using an objective and its camera. One can note that signal collection could have been done by fibre optics, but it gets the collection task more complicated. An USB camera is used in order to assist the positioning of the fibre and the objective, which fulfilling the same objective as the optical microscope, but from a perpendicular perspective.

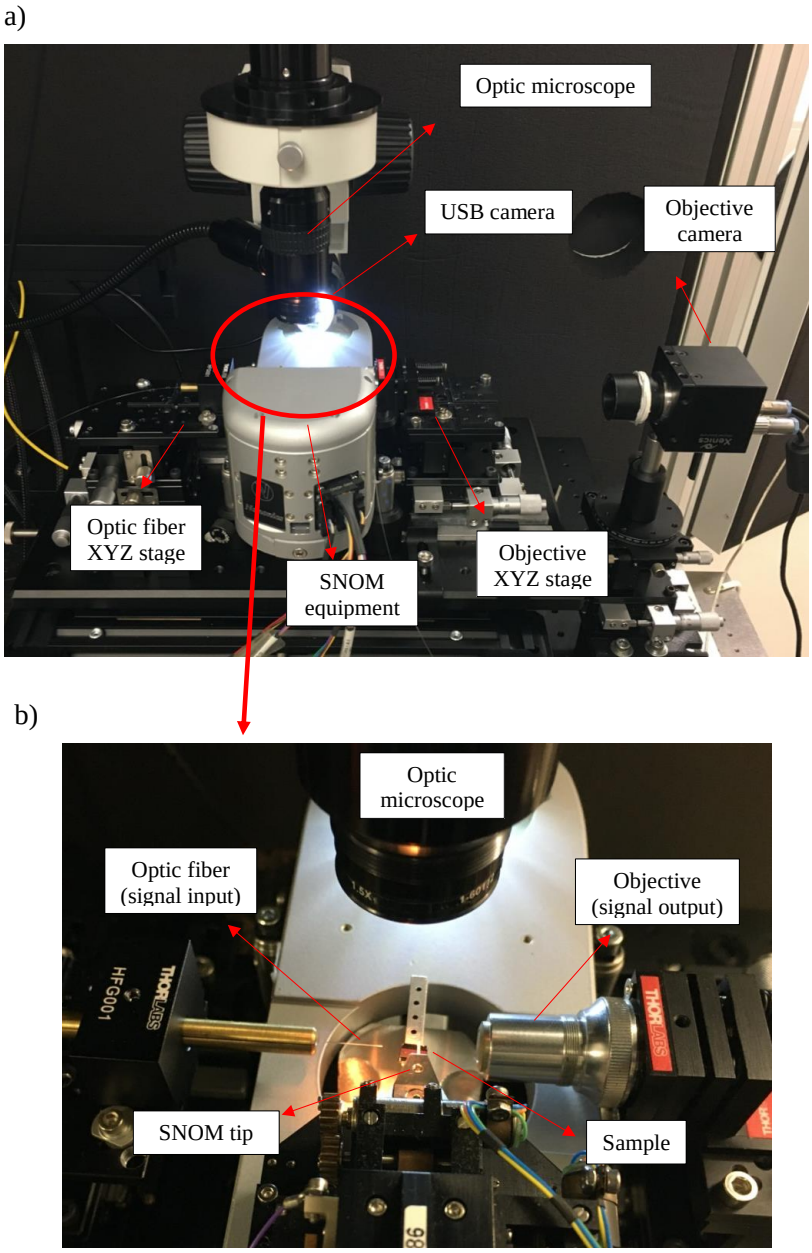

Figure 4.35: WERS-SNOM setup and components. a) WERS-SNOM overview. b) Zoom to sample positioning area.

Figure 4.35.b shows a more detailed view of the setup. As can be seen, the sample stage should be as thin as possible to allow the optical fibre to excite in the near field. Optic fiber and objective should

be aligned, and the SNOM probe is always at the top of the sample. The sample used here was a Si lithographed sample, with SiN wave-guides. This was used for verifying fiber-objective alignment, which is something challenging.

4.4.1 Optical fibre-target alignment for setup validation

For validating the setup, it should be considered the correct alignment between the optical fibre and the objective, as the basis of a correct performance resides in both accurate signal input and signal output collection. It is considered relevant to be mentioned that alignment is a highly challenging task, and that the alignment method used in this study is under development and is still being optimised. Figure 4.36.a shows the alignment configuration, while 4.36.b shows the result of a proper alignment. The success of the alignment is evaluated with the image provided by the objective camera, which has to present a circle of light in the centre of the image. This circle corresponds to the exit of the laser through the structure.

a)

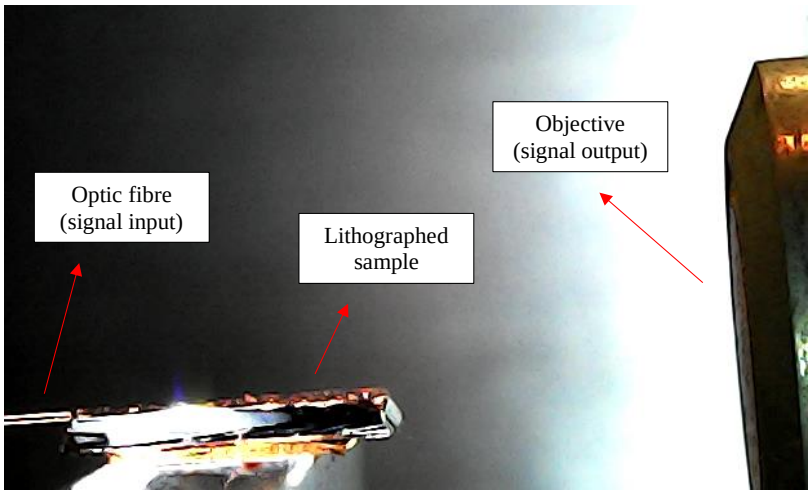

b)

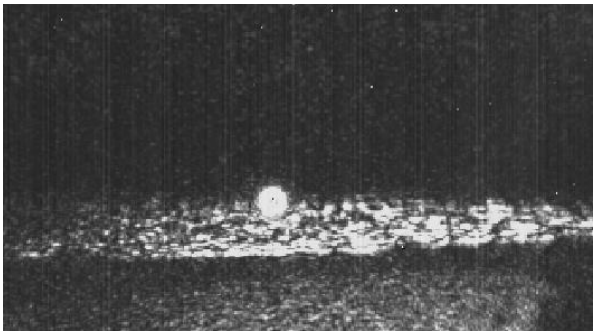

Figure 4.36: a) Optic fibre-objective alignment configuration. b) Objective camera image resulting from a proper alignment.

The new WERS-SNOM setup is and extremely promising equipment and optimised will provide a unique SAM characterisation method, combining two different ways of near-field excitation, a near and a far collection mode, a near and a far collection mode, and the possibility to perform surface topography measurements together with measurements of excitation modes of structures, all of which can collect the Raman signal in a guided mode. This work remains as ongoing work, as it requires more time than has been available for this work.

4.5 New structures simulation results

In this section the results of two simulations performed considering new plasmonic structures are presented. In this case, the aim is to simulate the behaviour of a structure with the highest possible EM enhancement at a frequency of around 1500 nm (Near Infrared or NIR). In this case, the function of the NIR would be analogous to that of the visible, used in previous simulations. It is necessary to emphasise that the THz ranges to be detected are those of the Mid innfrared (MIR) and Far infrared (FIR), not the NIR, which would serve as excitation of the structure.

As mentioned above, the structure response to visible and THz signals depends, among other things, on the size and composition of the NPs used. Theoretically, considering spherical NPs, larger NP sizes imply larger responses at lower frequencies. Therefore, for an optimal response in the NIR ranges, simulations have been performed considering larger NPs than those considered throughout the experimental part of this work, being of the order of microns. Therefore, the simulated structure is composed by: a Si wave-guide (not SiN, as they used to be) which dimensions are 3000 nm long, 500 nm wide and 200 nm high; an Au surface of 300 nm long, 500 nm wide and 10 nm high has been placed on the wave-guide surface; a dielectric material of the same Au surface dimensions (except for the high, which is 1 nm), which simulates simulate the SAM; a Si NP covered by Au (of sizes 1µm and 2µm, running 2 different simulat). The excitation range used was from 150 to 550 THz, covering the visible and near-infrared (NIR) range, at which the NPoM essential plasmonic resonance occurs.

Simulation 1: Si wave-guide and 1µm Si-Au NP

The first design consists of a structure based on the components described above, where the NPoM is composed of a gold patch on top of the guide and a 0.95 µm spherical Si NP coated with a 50 nm thickness Au layer. Figure 4.37 shows the resulting structure after implementing it in CST. The red squares located at the ends of the guide and above the NP simulate the excitation and signal collection ports. Port 1 is at the right end of the guide, port 2 is at the left end and port 3 is at the top of the NP. Port 1 is used as signal input, while ports 2 and 3 are used as output.

Nine probes were placed under the PN, right in the area of the SAM, one of them being in the centre of the PN and the others around it. This was done to check that the greatest EM confinement occurred in the area where the SAM and the NP are closest to each other. Figure 4.38 shows 9 plots, associated

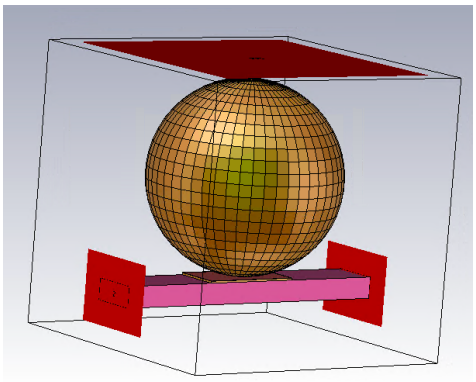

Figure 4.37: Hybrid NPoM-guide structure composed by 1 µm Si-AU NP and a gold patch located above the Si wave-guide.

with the signal from each of the 9 probes. The abscissa axis represents the wavelength, while the ordinate axis represents the electric field. It can be seen how the signal of the centre probe (which represents the closest proximity between the NP and the mirror) is of the order of twice as large as the signal of the other probes. In addition, the EM field shows a phenomenon of higher enhancement at wavelengths of 1300 nm and 1600 nm, these values being of the order of the expected but which could be optimised.

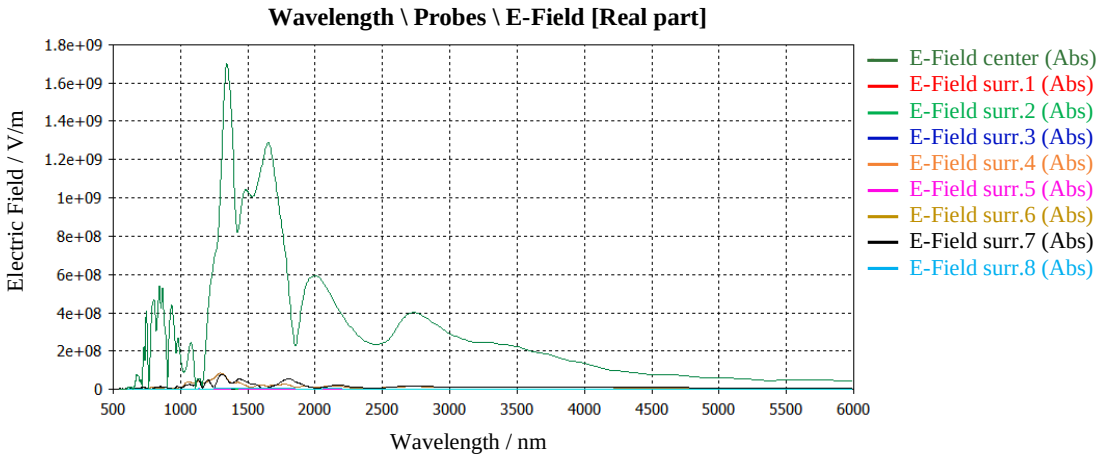

Figure 4.38: Graphic representation of the simulation 1 results. Wavelength-dependent variation of the magnetic field. Response of the 9 probes placed in the NPoM gap in the structure of Figure 4.37.

Merely for comparison purposes, Figure 4.39 shows the basis Si guide structure on which an 80 nm NP has been placed, the size of which is of the order in which simulations have been performed to date. A remarkable difference can be observed by comparing the structures of Figures 4.37 and Figure 4.39, which makes it therefore evident that the performance will be significantly different comparing both cases.

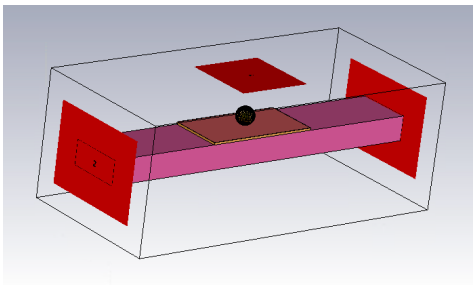

Figure 4.39: Structure of Si guide Si and NPoM. The size of the NP is 80 nm. Sizes of this order have been used throughout the work. The size of the rest of the components is the one used in the new simulations.

Simulation 2: Si wave-guide and 2µm NPoM

For the second simulation, a NP of 2 µm size was used. The objective was to maintain the rest of the other components with the same size as in simulation 1. However, Figure 4.40 shows how the input and output ports 1 and 2 are considerably further away from the ends of the guide than in the previous simulation. In addition, the mesh size of the simulation was 5 times larger than in the 1 µm case. This made this simulation temporarily non-viable, and no coherent results could be extracted from it.

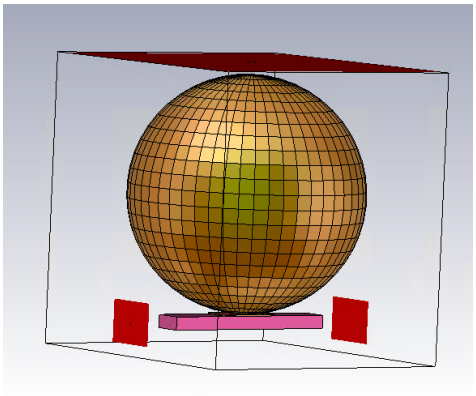

Figure 4.40: Hybrid NPoM-guide structure composed by 1 µm Si-AU NP and a gold patch located above the Si wave-guide.

Chapter 5

ONGOING WORK

In this work, results obtained from several lines of study have been presented, the aim of which converges in the characterization of molecular monolayers and study of photonic circuits viability for the production of integrated THz detectors. Some of these lines will continue to be investigated by the author of this study after the delivery of this work, which are mentioned below.

In order to compare the SERS effect produced by the NPoM structure, experiments will be carried out using square NPs instead of round ones, in order to extract new results that are more enhanced in different wavelength ranges depending on the shape of the NP. In addition, new slit-based plasmonic structures will also be functionalised with ABIZ, which have been shown in simulations to be useful for signal enhancement in guidance and to serve as an antenna for the THz signal.

Regarding the wave-guided Raman, WERS setup will be optimized in order to measure guided Raman. For this purpose, polyethylene (PE)-coated Si waveguide samples will be used, as the laser used in the assembly is of the order of 1500 nm wavelength and the PE has a Raman peak at the same wavelength. SNOM measurements will also be required, as well as near-field excitation of the guide vertically using the same technique.

Finally, simulations will be continued to be performed, using larger NP sizes than those used experimentally, in order to obtain new structures that will allow for an optimal up-conversion of the signal in a guided configuration.

Chapter 6

CONCLUSIONS

Several experimental methodologies have been implemented throughout the development of this work. For each of them, it is possible to draw several conclusions. These are exposed below.

Functionalization: From the results obtained after functionalizing the structures with BPT and ABIZ, it has been possible to draw several conclusions. First, **BPT** functionalization worked successfully on lithographed gold disks sample. Moreover, these samples were used to further validate the new NPs deposition method, called *Micro-contact printing*. However, this disks structure was not suitable for further guided Raman research, so this work continued on another line of lithographic samples. In addition, BPT molecular vibrations at THz are acceptable for up-conversion, but using other molecules can provide better results for THz optomechanical signal coupling, so other molecules were investigated to give better results in this range (ABIZ). Secondly, regarding functionalizaiton using **ABIZ** molecule, a new method for generating self-assembled molecular monolayers has been proposed and validated in this work, providing a stable, low-cost functionalization technique. In addition, using ABIZ molecules allows to perform the up-conversion of the THz signal in ranges of greater interest than BPT. With this molecule, lithographed SiN guides samples have been successfully functionalized. A paper manuscript is being prepared, as the results obtained are considered valuable to the research community. Protonation technique has also been used to increase the affinity of ABIZ for the surface of the NPs, thereby improving their binding.

NPs transfer: In this work, two NPs deposition techniques have been used. A **new NPs transfer technique (Micro-contact printing technique)** has been successfully employed and experimentally validated, providing a new methodology that is significantly more accurate than the so-called drop-casing methodology generally used. Additionally, NPs transfer has also been used to **characterize and validate functionalizations** performed with both BPT and ABIZ molecules, showing that these had been successfully carried out.

WERS-SNOM: A new excitation and measurement equipment has been set up that will allow guided Raman combined with SNOM measurements. As the aim is to achieve circuits that allow wave-guiding through them, new experimental set-ups are needed to accurately evaluate the performance

of nanophotonic guidance structures, and with the new WERS-SNOM setup these requirements can be covered. In addition, with this new circuit it will be possible to perform WERS, being able to excite the structures that are above the guide and detect the molecules that are also above it. A first approximation of the correct performance of this equipment has been tested by aligning the input and output with the guide sample, **showing that it has been assembled successfully**.

Simulations: Two simulations considering NP sizes in the order of 3 times the size normally considered have been performed. The first of them, where the NP size is 1 µm, has given satisfactory results, **showing that the EM field is enhanced nearly the area of interest**, showing that a NIR laser can also be used to excite plasmonic structures. Unfortunately, the simulation performed using 2 µm NP diverged, providing inconsistent results in extremely long timescales.

Ultimately, **each section of this work has contributed to the characterization of molecular monolayers on photonic nanostructures. Additionally, other lines of research have also been covered**, such as the creation of new functionalization and characterisation techniques and the simulation of new circuits to study their viability, making a more extensive contribution to the THOR project. Studying and characterizing other possible circuits and potential molecules SAMs is fundamental to ultimately developing these detectors. This work has therefore served as a basis for valuable future work.

Part II

Budget

Chapter 7

BUDGET

7.1 Introduction

This document provides a detailed analysis of the economic resources used to develop this project, taking into account the labour, machinery and materials used in each of the phases. In addition, a study of the market launch economic viability of nanophotonic THz detectors to the market is also reported.

The workforce consists of a tutor and a co-tutor, who keep the student's workflow under continuous supervision, and a fourth year biomedical engineering student. To simplify the budget calculation, only the contribution of the tutor's labour will be assumed, since each one was present in different phases of the project. The cost of tutor and student labour for the company is calculated by using equation 7.1.

$$Worker\,cost\ =\ Gross\,salary\ +\ Social\,security\,cost \tag{7.1}$$

The Social security cost is determined using percentages of the employee's gross salary. Considering: 23,6% is the contribution for common contingencies, 5,5 % the unemployment contributions for permanent contracts, 1% the contribution for accidents at work and occupational diseases for office workers, 0,6% the quotation for vocational training and 0,2% the contribution to the Wage Guarantee Fund (FOGASA), Social security cost is calculated in equation 7.2:

$$Social\,security\,cost\ =\ Gross\,salary\ \times\ (0,236\ +\ 0,055\,0,010+\ +0,006\ +\ 0,002) \tag{7.2}$$

Considering the holiday period and annual bonuses, it is estimated that the annual salary of an engineering student is 1100 euros, while the salary of the tutor as a university professor is around 3500 euros. The annual SSC or *Social Security Cost* for the biomedical engineering student (BES, eq. 7.3) and for the professor tutor (PF, eq. 7.4):

$$Annual\ SSC\ BES\ =\ 4.078,8\frac{€}{year} \tag{7.3}$$

$$Annual\ SSC\ PT\ =\ 12.978\frac{€}{year} \tag{7.4}$$

And the annual worker cost (BES and PT), in each case:

$$Annual\ BES\ cost\ = 1100\ \frac{€}{month}\ \times\ 12\ \times\ 4078,8\frac{€}{year} = 17.278,8\frac{€}{year} \tag{7.5}$$

$$Annual\ PT\ cost\ = 3500\ \frac{€}{month}\ \times\ 12\ \times\ 12978\frac{€}{year} = 54.978\frac{€}{year} \tag{7.6}$$

Discounting Sundays, Saturdays and public holidays, the working days in a year of 365 days are 224, 8 working hours each day, the hourly cost of each of the persons considered as labour remains:

$$Hourly\ BES\ cost\ = \frac{17.278,8\frac{€}{year}}{(224\frac{days}{year}) \times 8\frac{hours}{day}}\ = 9,64\frac{€}{hour} \tag{7.7}$$

$$Hourly\ PT\ cost\ = \frac{54.978\frac{€}{year}}{(224\frac{days}{year}) \times 8\frac{hours}{day}}\ = 30,68\frac{€}{hour} \tag{7.8}$$

Being 9,64 $\frac{€}{hour}$ for the hourly cost of the student, and 30,68$\frac{€}{hour}$ for the hourly cost of the student.

Considering the experimental characterization, all machinery used and provided by the Nanophotonics Technology Center has been attributed a cost of 45$\frac{€}{hour}$ per equipment. In addition, materials include the licensing of the software used, as well as the laboratory equipment and the basic material (Si and others). Finally, from the partial budgets, the total budget for material execution is obtained by adding a 13 % overheads and 6 % of industrial profit. 21 % VAT is added in order to obtain the total budget.

7.2 Detailed budget

The detailed budget was obtained using *Arquímedes* software, student version. It consists of the following tables:

- Table of labour cost (Table 1).
- Table of materials cost (Table 2).
- Table of machinery cost (Table 3).
- Table of unit price list cost (Table 4).
- Tables of Partial budget (Tables 5-10).
- Table of contractual implementation budget (Table 11).

Table 1. Labour cost table.

Labour cost

Page 1

Num.	Code	Labour designation	Price	Hours	Total
1	L.PT	Thesis Professor Tutor	30,680	115,500h	3.543,54
2	L.BES	Biomedical Engineering Student	9,640	343,000h	3.306,52
				Total labour:	6.850,06

Table 2. Machinery cost table.

Machinery cost

Page 1

Num.	Code	Machinery designation	Price	Quantity	Total
1	EQ.Lit	Lithography: Raith 150	500,000	1,000h	500,00
2	EQ.R	PMMA + Coater EVG 101 and Tepla PVA + Curing and Reveiling (Brewer Model)	150,000	1,000h	150,00
3	EQ.At	Attack with RIEICP	90,000	2,000h	180,00
4	EQ.CA	Contact Angle equipment, ramé-hart	45,000	21,000h	945,00
5	EQ.Laser	IR laser	45,000	20,000h	900,00
6	EQ.DLS	Dynamic Light Scattering equipment	45,000	0,500h	22,50
7	EQ.Oven	Oven	45,000	3,000h	135,00
8	EQ.3D	3D printer	45,000	4,000h	180,00
9	EQ.Ram	Spectrometer alpha300 RA (Raman-AFM), WITec	45,000	62,000h	2.790,00
10	EQ.SEM	SEM equipment	45,000	10,000h	450,00
11	EQ.SNOM	SNOM equipment	45,000	30,000h	1.350,00
12	EQ.SofWITec	Software Project 4.0, WITec (PC)	45,000	62,000h	2.790,00
13	EQ.Stamp	Stamp creation setup	45,000	6,000h	270,00
14	EQ.lap	Laptop	45,000	40,000u	1.800,00
				Total machinery:	12.462,50

Table 3. Materials cost table.

Materials cost

Page 1

Num.	Code	Material designation	Price	Quantity	Total
1	MAT.Scan	Scan Lense for Laser Scanning Microscopy, 800 to 1800 nm Wavelength Ramge	4.069,250	1,000u	4.069,25
2	MAT.sta	4-Axis Stages, Thin Profile, 62.5 mm Deck Height (THORLABS)	1.900,520	2,000u	3.801,04
3	MAT.Probe	SNOM probe 200 nm Cr-Au	1.598,500	1,000u	1.598,50
4	MAT.Stag	XYZ sample positioning	745,080	1,000u	745,08
5	MAT.Pol	Manual Fiber Polarization Controllers	323,370	1,000u	323,37
6	MAT.Waf	Wafer SiO	250,000	1,000u	250,00
7	MAT.PDMS	Sylgard 184 Silicon Elastomer kit, 1.1kg	245,670	1,000u	245,67
8	MAT.BPT	Biphenyl-4-thiol (752207, 1G), Merck	212,000	1,000u	212,00
9	MAT.Micr	Optical microscope	120,000	1,000u	120,00
10	MAT.NP150	Accurate Spherical Gold Nanoparticles 150nm (25 ml)	100,000	1,000u	100,00
11	MAT.NP60	Accurate Spherical Gold Nanoparticles 60nm (25 ml)	100,000	1,000u	100,00
12	MAT.ABIZ	5-Amino-2-Mercaptobenzimidazole (536067, 25 G), Merck	90,000	1,000u	90,00
13	MAT.Pap	Parafilm 100 mm x 38 m	68,000	1,000u	68,00
14	MAT.S	Scale	59,000	2,000u	118,00
15	MAT.CST	CST STUDIO SUITE	45,000	33,000h	1.485,00
16	MAT.USB	USB camera	35,800	1,000u	35,80
17	MAT.Et	Absolute ethanol	28,800	1,000L	28,80
18	MAT.Off	Microsoft Office 365 Licence	16,000	3,000u	48,00
19	MAT.Lab	Lab coat	15,000	1,000u	15,00
20	MAT.Win	Windows 10 Licence	7,400	1,000u	7,40
21	MAT.Glo	Nitrile gloves pack	5,920	9,000u	53,28
22	MAT.Ext	Extractor hood	2,100	1,000h	2,10
23	MAT.Vess	Glass vessel	1,700	3,000u	5,10
24	MAT.Wat	MiliQ water	1,250	1,000L	1,25
25	MAT.Fib	FIbre optic	0,600	7,000m	4,20
26	MAT.Syr	5 ml Syringe	0,250	6,000u	1,50
				Total materials:	13.528,34

Table 4. Unit price cost table.

Nº	Designation			Import	
				Partial (Euros)	Total (Euros)
	1 PROJECT DEFINITION				
1.1	u Initial meeting with tutor				
	(Labour)				
L.BES	Biomedical Engineering Student	1,500 h	9,640	14,46	
L.PT	Thesis Professor Tutor	1,500 h	30,680	46,02	
			Total	60,480	
					60,48
1.2	u Planning tasks meeting				
	(Labour)				
L.BES	Biomedical Engineering Student	2,000 h	9,640	19,28	
L.PT	Thesis Professor Tutor	2,000 h	30,680	61,36	
			Total	80,640	
					80,64
	2 STATE-OF-THE-ART INVESTIGATION				
2.1	u State-of-the-art investigation				
	(Mano de obra)				
L.BES	Biomedical Engineering Student	36,000 h	9,640	347,04	
L.PT	Thesis Professor Tutor	5,000 h	30,680	153,40	
	(Materiales)				
MAT.Off	Microsoft Office 365 Licence	1,000 u	16,000	16,00	
MAT.Win	Windows 10 Licence	1,000 u	7,400	7,40	
			Total	523,840	
					523,84
2.2	u Programme management training				
	(Mano de obra)				
L.BES	Biomedical Engineering Student	6,000 h	9,640	57,84	
L.PT	Thesis Professor Tutor	6,000 h	30,680	184,08	
	(Maquinaria)				
EQ.CA	Contact Angle equipment, ramé-hart	1,000 h	45,000	45,00	
EQ.Ram	Spectrometer alpha300 RA (Raman-AFM), WI…	2,000 h	45,000	90,00	
EQ.Sof…	Software Project 4.0, WITec (PC)	3,000 h	45,000	135,00	
			Total	511,920	
					511,92
	3 THEORETICAL ANALYSIS AND SAM CHARACTERIZATION				
3.1	u Structures design and manufacture				
	(Maquinaria)				
EQ.At	Attack with RIEICP	2,000 h	90,000	180,00	
EQ.Lit	Lithography: Raith 150	1,000 h	500,000	500,00	
EQ.R	PMMA + Coater EVG 101 and Tepla PVA + Cu…	1,000 h	150,000	150,00	
	(Materiales)				
MAT.CST	CST STUDIO SUITE	3,000 h	45,000	135,00	
MAT.Waf	Wafer SiO	1,000 u	250,000	250,00	
			Total	1.215,000	
					1.215,00

Price list

Nº	Designation			Import Partial (Euros)	Import Total (Euros)
3.2	u Structures surface functionalization				
	(Labour)				
L.BES	Biomedical Engineering Student	18,000 h	9,640	173,52	
L.PT	Thesis Professor Tutor	9,000 h	30,680	276,12	
	(Materials)				
MAT.ABIZ	5-Amino-2-Mercaptobenzimidazole (536067,…	1,000 u	90,000	90,00	
MAT.BPT	Biphenyl-4-thiol (752207, 1G), Merck	1,000 u	212,000	212,00	
MAT.Et	Absolute ethanol	1,000 L	28,800	28,80	
MAT.Ext	Extractor hood	1,000 h	2,100	2,10	
MAT.Glo	Nitrile gloves pack	6,000 u	5,920	35,52	
MAT.Lab	Lab coat	1,000 u	15,000	15,00	
MAT.N…	Accurate Spherical Gold Nanoparticles 15…	1,000 u	100,000	100,00	
MAT.N…	Accurate Spherical Gold Nanoparticles 60…	1,000 u	100,000	100,00	
MAT.Pap	Parafilm 100 mm x 38 m	1,000 u	68,000	68,00	
MAT.S	Scale	1,000 u	59,000	59,00	
MAT.Syr	5 ml Syringe	6,000 u	0,250	1,50	
MAT.Vess	Glass vessel	3,000 u	1,700	5,10	
MAT.Wat	MiliQ water	1,000 L	1,250	1,25	
			Total	1.167,910	
					1.167,91
3.3	u Stamp creation				
	(Labour)				
L.BES	Biomedical Engineering Student	10,000 h	9,640	96,40	
L.PT	Thesis Professor Tutor	6,000 h	30,680	184,08	
	(Machinery)				
EQ.Oven	Oven	3,000 h	45,000	135,00	
EQ.Stamp	Stamp creation setup	6,000 h	45,000	270,00	
	(Materials)				
MAT.Glo	Nitrile gloves pack	3,000 u	5,920	17,76	
MAT.P…	Sylgard 184 Silicon Elastomer kit, 1.1kg	1,000 u	245,670	245,67	
MAT.S	Scale	1,000 u	59,000	59,00	
			Total	1.007,910	
					1.007,91
3.4	u SAMs and structures characterization				
	(Labour)				
L.BES	Biomedical Engineering Student	130,500 h	9,640	1.258,02	
L.PT	Thesis Professor Tutor	50,500 h	30,680	1.549,34	
	(Machinery)				
EQ.CA	Contact Angle equipment, ramé-hart	20,000 h	45,000	900,00	
EQ.DLS	Dynamic Light Scattering equipment	0,500 h	45,000	22,50	
EQ.Ram	Spectrometer alpha300 RA (Raman-AFM), WI…	60,000 h	45,000	2.700,00	
EQ.SEM	SEM equipment	10,000 h	45,000	450,00	
EQ.Sof…	Software Project 4.0, WITec (PC)	40,000 h	45,000	1.800,00	
			Total	8.679,860	
					8.679,86
3.5	u Data processing				
	(Labour)				
L.BES	Biomedical Engineering Student	9,000 h	9,640	86,76	
L.PT	Thesis Professor Tutor	4,000 h	30,680	122,72	
	(Machinery)				
EQ.Sof…	Software Project 4.0, WITec (PC)	9,000 h	45,000	405,00	
			Total	614,480	
					614,48

Price list						
Nº	Designation				Import	
					Partial (Euros)	Total (Euros)
3.6	u Results interpretation					
	(Labour)					
L.BES	Biomedical Engineering Student	10,000	h	9,640	96,40	
L.PT	Thesis Professor Tutor	4,000	h	30,680	122,72	
	(Machinery)					
EQ.Sof…	Software Project 4.0, WITec (PC)	10,000	h	45,000	450,00	
				Total	669,120	
						669,12
	4 WERS ASSEMBLY					
4.1	u Theoretical viability study					
	(Labour)					
L.BES	Biomedical Engineering Student	3,000	h	9,640	28,92	
L.PT	Thesis Professor Tutor	1,500	h	30,680	46,02	
				Total	74,940	
						74,94
4.2	u WERS-SNOM assembly					
	(Labour)					
L.BES	Biomedical Engineering Student	40,000	h	9,640	385,60	
L.PT	Thesis Professor Tutor	20,000	h	30,680	613,60	
	(Machinery)					
EQ.3D	3D printer	4,000	h	45,000	180,00	
EQ.Laser	IR laser	20,000	h	45,000	900,00	
EQ.SNOM	SNOM equipment	30,000	h	45,000	1.350,00	
EQ.lap	Laptop	40,000	u	45,000	1.800,00	
	(Materials)					
MAT.Fib	FIbre optic	7,000	m	0,600	4,20	
MAT.Micr	Optical microscope	1,000	u	120,000	120,00	
MAT.Pol	Manual Fiber Polarization Controllers (T…	1,000	u	323,370	323,37	
MAT.Pr…	SNOM probe 200 nm Cr-Au	1,000	u	1.598,500	1.598,50	
MAT.Scan	Scan Lense for Laser Scanning Microscopy…	1,000	u	4.069,250	4.069,25	
MAT.Stag	Large-Area Translation Stage (THORLABS)	1,000	u	745,080	745,08	
MAT.USB	USB camera	1,000	u	35,800	35,80	
MAT.sta	4-Axis Stages, Thin Profile, 62.5 mm Dec…	2,000	u	1.900,520	3.801,04	
				Total	15.926,440	
						15.926,44
	5 SIMULATION STUDIES					
5.1	u Simmulation implementation					
	(Labour)					
L.BES	Biomedical Engineering Student	30,000	h	9,640	289,20	
	(Materials)					
MAT.CST	CST STUDIO SUITE	30,000	h	45,000	1.350,00	
				Total	1.639,200	
						1.639,20
5.2	u Results interpretation					
	(Labour)					
L.BES	Biomedical Engineering Student	5,000	h	9,640	48,20	
				Total	48,200	
						48,20
	6 WRITING AND THESIS LECTURE					

Price list

Nº	Designation			Import Partial (Euros)	Import Total (Euros)
6.1	u Writing documents				
	(Labour)				
L.BES	Biomedical Engineering Student	30,000 h	9,640	289,20	
	(Materials)				
MAT.Off	Microsoft Office 365 Licence	1,000 u	16,000	16,00	
			Total	305,200	
					305,20
6.2	u Documents review				
	(Labour)				
L.BES	Biomedical Engineering Student	4,000 h	9,640	38,56	
L.PT	Thesis Professor Tutor	6,000 h	30,680	184,08	
			Total	222,640	
					222,64
6.3	u Lecture preparation				
	(Labour)				
L.BES	Biomedical Engineering Student	8,000 h	9,640	77,12	
	(Materials)				
MAT.Off	Microsoft Office 365 Licence	1,000 u	16,000	16,00	
			Total	93,120	
					93,12

Valencia, May 2022
Biomedical Engineer

María Camarena Pérez

Table 5. Partial Budget num 1.

Partial Budget nº 1 PROJECT DEFINITION

Nº	Ud	Description		Measure	Price	Import
1.1	U	Initial meeting with tutor				
			Total u :	1,00	60,48	**60,48**
1.2	U	Planning tasks meeting				
			Total u :	1,00	80,64	**80,64**
		Total Partial Budget nº 1 PROJECT DEFINITION:				**141,12**

Table 6. Partial Budget num 2.

Partial Budget nº 2 STATE-OF-THE-ART INVESTIGATION

Nº	Ud	Description		Measure	Price	Import
2.1	U	State-of-the-art investigation				
			Total u :	1,00	523,84	**523,84**
2.2	U	Programme management training				
			Total u :	1,00	511,92	**511,92**
		Total Partial Budget nº 2 STATE-OF-THE-ART INVESTIGATION :				**1.035,76**

Table 7. Partial Budget num 3.

Partial Budget nº 3 THEORETICAL ANALYSIS AND SAM CHARACTERIZATION

Nº	Ud	Description		Measure	Price	Import
3.1	U	Structures design and manufacture				
			Total u :	1,00	1.215,00	**1.215,00**
3.2	U	Structures surface functionalization				
			Total u :	1,00	1.167,91	**1.167,91**
3.3	U	Stamp creation				
			Total u :	1,00	1.007,91	**1.007,91**
3.4	U	SAMs and structures characterization				
			Total u :	1,00	8.679,86	**8.679,86**
3.5	U	Data processing				
			Total u :	1,00	614,48	**614,48**
3.6	U	Results interpretation				
			Total u :	1,00	669,12	**669,12**
Total Partial Budget nº 3 THEORETICAL ANALYSIS AND SAM CHARACTERIZ...						**13.354,28**

Table 8. Partial Budget num 4.

Partial Budget nº 4 WERS ASSEMBLY

Nº	Ud	Description		Measure	Price	Import
4.1	U	Theoretical viability study				
			Total u :	1,00	74,94	**74,94**
4.2	U	WERS-SNOM assembly				
			Total u :	1,00	15.926,44	**15.926,44**
		Total Partial Budget nº 4 WERS ASSEMBLY :				**16.001,38**

Table 9. Partial Budget num 5.

Partial Budget nº 5 SIMULATION STUDIES

Nº	Ud	Description		Measure	Price	Import
5.1	U	Simmulation implementation				
			Total u :	1,00	1.639,20	**1.639,20**
5.2	U	Results interpretation				
			Total u :	1,00	48,20	**48,20**
		Total Partial Budget nº 5 SIMULATION STUDIES :				**1.687,40**

Table 10. Partial Budget num 6.

Partial Budget nº 6 WRITING AND THESIS LECTURE

Nº	Ud	Description		Measure	Price	Import
6.1	U	Writing documents				
			Total u :	1,00	305,20	**305,20**
6.2	U	Documents review				
			Total u :	1,00	222,64	**222,64**
6.3	U	Lecture preparation				
			Total u :	1,00	93,12	**93,12**
		Total Partial Budget nº 6 WRITING AND THESIS LECTURE :				**620,96**

Table 11. Contractual implementation budget.

Project: THESIS BUDGET

Chapter	Import
1 PROJECT DEFINITION	**141,12**
2 STATE-OF-THE-ART INVESTIGATION	**1.035,76**
3 THEORETICAL ANALYSIS AND SAM CHARACTERIZATION	**13.354,28**
4 WERS ASSEMBLY	**16.001,38**
5 SIMULATION STUDIES	**1.687,40**
6 WRITING AND THESIS LECTURE	**620,96**
Material execution budget	**32.840,90**
15% overheads	4.926,14
6% industrial profit	1.970,45
Sum	**39.737,49**
21% VAT	8.344,87
Contractual execution budget	**48.082,36**

The contract execution budget amounts to the aforementioned sum of FORTY-EIGHT THOUSAND EIGHTY-TWO EUROS AND THIRTY-SIX CENTS.

Valencia, May 2022
Biomedical Engineer

María Camarena Pérez

7.3 Cost of an integrated photonic THz sensor

As stated, the aim of this work is to contribute to the THOR project, whose objective is to develop structures that allow for the detection of signals at THz and which also provide for both on-chip integration and effective performance at room temperature. This can also be combined with low cost by using the optomechanical properties of the structures. To provide an overview of how much one of these integrated sensors would cost, an economic analysis has been carried out in this section, taking into account the materials and techniques required for their manufacture.

The estimated costs associated with each process and material are presented below:

- Silicon on insulator (SOI) 176.7 cm^2 wafer: 250 €
- PMMA resin deposition process, using Coater EVG 101 and Tecla PVA, curing and revealing with Brewer Model: 150 €/wafer
- 5 hours Ebeam exposure: 2500 €.
- Attack with ICP-RIE: 90 €/ wafer
- ABIZ molecule: 90 €/ 25 g
- Accurate™ Spherical Gold Nanoparticles 60 nm: 100 €/ 25 ml
- Accurate™ Spherical Gold Nanoparticles 150 nm: 100 €/ 25 ml

The costs for one wafer in laboratory conditions would be 2990 €. Taking into consideration that an assembled chip measures 6 cm^2, one can consider the ratio 176.7 cm^2 / 6 cm^2 = 29.45, where

29.45 would be the number of chips generated from a single wafer if all the material is utilized. As the wafer is round and the chips are square, this ideal case is not possible, and it has been considered an approximation that the number of microchips that would be produced on a wafer would be 21 chips per wafer. This generates a manufacturing cost for a single chip of 2990 €/ 21 chips = **142.38 €/chip under laboratory conditions**. In addition, considering that per micro chip would be used 10 µl of gold NPs, and that the price of 1 ml would be 100€/25ml = 4 €/ml, the cost of adding NPs to the structure would be 0.01 ml× 4€/ml = 0.04 €= 4 cts. Thus, the price per chip assembled **under laboratory conditions amounts to 142.42 €/chip.** However, **taking into account mass production, this could be reduced to values of less than 1€/chip.**

Bibliography

[1] SS Dhillon, MS Vitiello, EH Linfield, AG Davies, Matthias C Hoffmann, John Booske, Claudio Paoloni, M Gensch, Peter Weightman, GP Williams, et al. The 2017 terahertz science and technology roadmap. *Journal of Physics D: Applied Physics*, 50(4):043001, 2017.

[2] Shian U Hwu, Kanishka B deSilva, and Cindy T Jih. Terahertz (thz) wireless systems for space applications. In *2013 IEEE Sensors Applications Symposium Proceedings*, pages 171–175. IEEE, 2013.

[3] Liqun Wang and Boris Mizaikoff. Application of multivariate data-analysis techniques to biomedical diagnostics based on mid-infrared spectroscopy. *Analytical and bioanalytical chemistry*, 391(5):1641–1654, 2008.

[4] Andrea G Markelz and Daniel M Mittleman. Perspective on terahertz applications in bioscience and biotechnology. *ACS Photonics*, 2022.

[5] Yeran Bai, Jiaze Yin, and Ji-Xin Cheng. Bond-selective imaging by optically sensing the mid-infrared photothermal effect. *Science Advances*, 7(20):eabg1559, 2021.

[6] Irina T Sorokina and Konstantin L Vodopyanov. *Solid-state mid-infrared laser sources*, volume 89. Springer Science & Business Media, 2003.

[7] Antoni Rogalski. *Infrared and terahertz detectors*. CRC Press, 2019.

[8] F Sizov. Terahertz radiation detectors: the state-of-the-art. *Semiconductor Science and Technology*, 33(12):123001, 2018.

[9] Antoni Rogalski. Infrared detectors: an overview. *Infrared physics & technology*, 43(3-5):187–210, 2002.

[10] HUI Wang, Daniel W Brandl, Peter Nordlander, and Naomi J Halas. Plasmonic nanostructures: artificial molecules. *Accounts of chemical research*, 40(1):53–62, 2007.

[11] Benedikt Schwarz, Peter Reininger, Daniela Ristanić, Hermann Detz, Aaron Maxwell Andrews, Werner Schrenk, and Gottfried Strasser. Monolithically integrated mid-infrared lab-on-a-chip using plasmonics and quantum cascade structures. *Nature communications*, 5(1):1–7, 2014.

[12] Philippe Roelli, Christophe Galland, Nicolas Piro, and Tobias J Kippenberg. Molecular cavity optomechanics as a theory of plasmon-enhanced raman scattering. *Nature nanotechnology*, 11(2):164–169, 2016.

[13] Angelos Xomalis, Xuezhi Zheng, Rohit Chikkaraddy, Zsuzsanna Koczor-Benda, Ermanno Miele, Edina Rosta, Guy AE Vandenbosch, Alejandro Martínez, and Jeremy J Baumberg. Detecting mid-infrared light by molecular frequency upconversion in dual-wavelength nanoantennas. *Science*, 374(6572):1268–1271, 2021.

[14] Wen Chen, Philippe Roelli, Huatian Hu, Sachin Verlekar, Sakthi Priya Amirtharaj, Angela I Barreda, Tobias J Kippenberg, Miroslavna Kovylina, Ewold Verhagen, Alejandro Martínez, et al. Continuous-wave frequency upconversion with a molecular optomechanical nanocavity. *Science*, 374(6572):1264–1267, 2021.

[15] Zongwei Xu, Zhongdu He, Ying Song, Xiu Fu, Mathias Rommel, Xichun Luo, Alexander Hartmaier, Junjie Zhang, and Fengzhou Fang. Topic review: Application of raman spectroscopy characterization in micro/nano-machining. *Micromachines*, 9(7):361, 2018.

[16] Daniel C Harris and Michael D Bertolucci. *Symmetry and spectroscopy: an introduction to vibrational and electronic spectroscopy*. Courier Corporation, 1989.

[17] Ewen Smith and Geoffrey Dent. *Modern Raman spectroscopy: a practical approach*. John Wiley & Sons, 2019.

[18] J González and J Marquina. Fundamentos de la dispersión raman: Algunos efectos de las altas presiones. In *Materia a alta presión: fundamentos y aplicaciones*, pages 163–182. Servicio de Publicaciones, 2011.

[19] Ruchita S Das and YK Agrawal. Raman spectroscopy: recent advancements, techniques and applications. *Vibrational spectroscopy*, 57(2):163–176, 2011.

[20] Dana Cialla, Sibyll Pollok, Carolin Steinbrücker, Karina Weber, and Jürgen Popp. Sers-based detection of biomolecules. *Nanophotonics*, 3(6):383–411, 2014.

[21] Ramón A Alvarez-Puebla and Luis M Liz-Marzán. Sers detection of small inorganic molecules and ions. *Angewandte Chemie International Edition*, 51(45):11214–11223, 2012.

[22] J Wollschlaeger and KO Möller. Ocean in situ sensors: New developments in biological sensors-plankton needs and methods. In *Challenges and Innovations in Ocean In Situ Sensors-Measuring Inner Ocean Processes and Health in the Digital Age*, pages 81–94. Elsevier, 2019.

[23] Paul L Stiles, Jon A Dieringer, Nilam C Shah, and Richard P Van Duyne. Surface-enhanced raman spectroscopy. *Annu. Rev. Anal. Chem.*, 1:601–626, 2008.

[24] Sebastian Schlücker. Surface-enhanced raman spectroscopy: Concepts and chemical applications. *Angewandte Chemie International Edition*, 53(19):4756–4795, 2014.

[25] Katherine A Willets and Richard P Van Duyne. Localized surface plasmon resonance spectroscopy and sensing. *Annu. Rev. Phys. Chem.*, 58:267–297, 2007.

[26] Janina Kneipp, Harald Kneipp, and Katrin Kneipp. Sers—a single-molecule and nanoscale tool for bioanalytics. *Chemical Society Reviews*, 37(5):1052–1060, 2008.

[27] BO Skadtchenko and R Aroca. Surface-enhanced raman scattering of p-nitrothiophenol: Molecular vibrations of its silver salt and the surface complex formed on silver islands and colloids. *Spectrochimica Acta Part A: Molecular and Biomolecular Spectroscopy*, 57(5):1009–1016, 2001.

[28] Ali Raza, Stéphane Clemmen, Pieter Wuytens, Muhammad Muneeb, Michiel Van Daele, Jolien Dendooven, Christophe Detavernier, Andre Skirtach, and Roel Baets. Ald assisted nanoplasmonic slot waveguide for on-chip enhanced raman spectroscopy. *APL Photonics*, 3(11):116105, 2018.

[29] Xiangxian Wang, Yuan Wu, Xiaolei Wen, Jiankai Zhu, Xuelin Bai, Yunping Qi, and Hua Yang. Surface plasmons and sers application of au nanodisk array and au thin film composite structure. *Optical and Quantum Electronics*, 52(5):1–11, 2020.

[30] Angela I Barreda, Mario Zapata-Herrera, Isabelle M Palstra, Laura Mercadé, Javier Aizpurua, A Femius Koenderink, and Alejandro Martínez. Hybrid photonic-plasmonic cavities based on the nanoparticle-on-a-mirror configuration. *Photonics Research*, 9(12):2398–2419, 2021.

[31] Felix Benz, Rohit Chikkaraddy, Andrew Salmon, Hamid Ohadi, Bart De Nijs, Jan Mertens, Cloudy Carnegie, Richard W Bowman, and Jeremy J Baumberg. Sers of individual nanoparticles on a mirror: size does matter, but so does shape. *The journal of physical chemistry letters*, 7(12):2264–2269, 2016.

[32] Nuttawut Kongsuwan, Angela Demetriadou, Matthew Horton, Rohit Chikkaraddy, Jeremy J Baumberg, and Ortwin Hess. Plasmonic nanocavity modes: From near-field to far-field radiation. *ACS Photonics*, 7(2):463–471, 2020.

[33] Syed Mubeen, Shunping Zhang, Namhoon Kim, Seungjoon Lee, Stephan Krämer, Hongxing Xu, and Martin Moskovits. Plasmonic properties of gold nanoparticles separated from a gold mirror by an ultrathin oxide. *Nano letters*, 12(4):2088–2094, 2012.

[34] Rohit Chikkaraddy, Xuezhi Zheng, Felix Benz, Laura J Brooks, Bart De Nijs, Cloudy Carnegie, Marie-Elena Kleemann, Jan Mertens, Richard W Bowman, Guy AE Vandenbosch, et al. How ultranarrow gap symmetries control plasmonic nanocavity modes: from cubes to spheres in the nanoparticle-on-mirror. *Acs Photonics*, 4(3):469–475, 2017.

[35] C Tserkezis, Ruben Esteban, Daniel O Sigle, Jan Mertens, Lars O Herrmann, Jeremy J Baumberg, and Javier Aizpurua. Hybridization of plasmonic antenna and cavity modes: Extreme optics of nanoparticle-on-mirror nanogaps. *Physical Review A*, 92(5):053811, 2015.

[36] Li Li, Tanya Hutter, Ullrich Steiner, and Sumeet Mahajan. Single molecule sers and detection of biomolecules with a single gold nanoparticle on a mirror junction. *Analyst*, 138(16):4574–4578, 2013.

[37] Rohit Chikkaraddy, Bart De Nijs, Felix Benz, Steven J Barrow, Oren A Scherman, Edina Rosta, Angela Demetriadou, Peter Fox, Ortwin Hess, and Jeremy J Baumberg. Single-molecule strong coupling at room temperature in plasmonic nanocavities. *Nature*, 535(7610):127–130, 2016.

[38] Florian Marquardt and Steven M Girvin. Optomechanics. *Physics*, 2:40, 2009.

[39] Martino Giaquinto, Anna Aliberti, Alberto Micco, Federica Gambino, Menotti Ruvo, Armando Ricciardi, and Andrea Cusano. Cavity-enhanced lab-on-fiber technology: toward advanced biosensors and nano-opto-mechanical active devices. *ACS Photonics*, 6(12):3271–3280, 2019.

[40] Moritz Forsch, Robert Stockill, Andreas Wallucks, Igor Marinković, Claus Gärtner, Richard A Norte, Frank van Otten, Andrea Fiore, Kartik Srinivasan, and Simon Gröblacher. Microwave-to-optics conversion using a mechanical oscillator in its quantum ground state. *Nature Physics*, 16(1):69–74, 2020.

[41] Hyeong-Ryeol Park, Kwang Jun Ahn, Sanghoon Han, Young-Mi Bahk, Namkyoo Park, and Dai-Sik Kim. Colossal absorption of molecules inside single terahertz nanoantennas. *Nano letters*, 13(4):1782–1786, 2013.

[42] Muhammad A Othman, Yasser M Sabry, Mohamed Sadek, Ismail M Nassar, and Diaa A Khalil. Transmission-enabled fiber fabry–perot cavity based on a deeply etched slotted micromirror. *Applied optics*, 57(16):4610–4617, 2018.

[43] Markus Aspelmeyer, Tobias J Kippenberg, and Florian Marquardt. Cavity optomechanics. *Reviews of Modern Physics*, 86(4):1391, 2014.

[44] Wenyan Yu, Wei C Jiang, Qiang Lin, and Tao Lu. Cavity optomechanical spring sensing of single molecules. *Nature communications*, 7(1):1–9, 2016.

[45] Yuan Zhang, Ruben Esteban, Roberto A Boto, Mattin Urbieta, Xabier Arrieta, ChongXin Shan, Shuzhou Li, Jeremy J Baumberg, and Javier Aizpurua. Addressing molecular optomechanical effects in nanocavity-enhanced raman scattering beyond the single plasmonic mode. *Nanoscale*, 13(3):1938–1954, 2021.

[46] Philippe Roelli, Diego Martin-Cano, Tobias J Kippenberg, and Christophe Galland. Molecular platform for frequency upconversion at the single-photon level. *Physical Review X*, 10(3):031057, 2020.

[47] Zsuzsanna Koczor-Benda, Philippe Roelli, Christophe Galland, and Edina Rosta. Molecular vibration explorer: an online database and toolbox for surface-enhanced frequency conversion, infrared and raman spectroscopy. *arXiv preprint arXiv:2112.11237*, 2021.

[48] Mohamed A Ettabib, Almudena Marti, Zhen Liu, Bethany M Bowden, Michalis N Zervas, Philip N Bartlett, and James S Wilkinson. Waveguide enhanced raman spectroscopy for biosensing: A review. *ACS sensors*, 6(6):2025–2045, 2021.

[49] Zilong Wang, Michalis N Zervas, Philip N Bartlett, and James S Wilkinson. Surface and waveguide collection of raman emission in waveguide-enhanced raman spectroscopy. *Optics Letters*, 41(17):4146–4149, 2016.

[50] Javier Martí Sendra. Fabricación de nanoestructuras y nanomateriales. *UPV*, 2016.

[51] Ryan D Mellor, Andreas G Schätzlein, and Ijeoma F Uchegbu. Development of biofunctionalized, raman responsive, and potentially excretable gold nanoclusters. *Nanomaterials*, 11(9):2181, 2021.

[52] Tommaso Ferri, Daniele Frasca, Olimpia Arias de Fuentes, Roberto Santucci, and Marco Frasconi. Spatially oriented and reversible surface assembly of single-walled carbon nanotubes: A strategy based on π–π interactions. *Angewandte Chemie International Edition*, 50(31):7074–7078, 2011.

[53] National Center for Biotechnology Information. Biphenyl-4-thiol anion. *PubChem Compound Summary for CID 7161093*, Retrieved May 5, 2022 from https://pubchem.ncbi.nlm.nih.gov/compound/Biphenyl-4-thiol-anion, 2022.

[54] National Center for Biotechnology Information. 5-amino-2-mercaptobenzimidazole. *PubChem Compound Summary for CID 2734002*, Retrieved May 6, 2022 from https://pubchem.ncbi.nlm.nih.gov/compound/5-Amino-2-mercaptobenzimidazole, 2022.

[55] R Karimi Shervedani, F Yaghoobi, and M Bagherzadeh. Electrocatalytic determination of hydroquinone with mn+ modified gold-5-amino-2-mercaptobenzimidazole self-assembled monolayer electrodes. *Journal of the Iranian Chemical Society*, 6(1):104–112, 2009.

[56] J Christopher Love, Lara A Estroff, Jennah K Kriebel, Ralph G Nuzzo, and George M Whitesides. Self-assembled monolayers of thiolates on metals as a form of nanotechnology. *Chemical reviews*, 105(4):1103–1170, 2005.

[57] George Socrates. *Infrared and Raman characteristic group frequencies: tables and charts*. John Wiley & Sons, 2004.